PHYSICAL REVIEW D **93,** 122003 (2016)

GW150914: First results from the search for binary black hole coalescence with Advanced LIGO

B. P. Abbott *et al.*[*]
(LIGO Scientific Collaboration and Virgo Collaboration)
(Received 9 March 2016; published 7 June 2016)

On September 14, 2015, at 09:50:45 UTC the two detectors of the Laser Interferometer Gravitational-Wave Observatory (LIGO) simultaneously observed the binary black hole merger GW150914. We report the results of a matched-filter search using relativistic models of compact-object binaries that recovered GW150914 as the most significant event during the coincident observations between the two LIGO detectors from September 12 to October 20, 2015 GW150914 was observed with a matched-filter signal-to-noise ratio of 24 and a false alarm rate estimated to be less than 1 event per 203000 years, equivalent to a significance greater than 5.1 σ.

DOI: 10.1103/PhysRevD.93.122003

I. INTRODUCTION

On September 14, 2015, at 09:50:45 UTC the LIGO Hanford, Washington, and Livingston, Louisiana, observatories detected a signal from the binary black hole merger GW150914 [1]. The initial detection of the event was made by low-latency searches for generic gravitational-wave transients [2]. We report the results of a matched-filter search using relativistic models of compact binary coalescence waveforms that recovered GW150914 as the most significant event during the coincident observations between the two LIGO detectors from September 12 to October 20, 2015. This is a subset of the data from Advanced LIGO's first observational period that ended on January 12, 2016.

The binary coalescence search targets gravitational-wave emission from compact-object binaries with individual masses from 1 $M_\odot$ to 99 $M_\odot$, total mass less than 100 $M_\odot$ and dimensionless spins up to 0.99. The search was performed using two independently implemented analyses, referred to as PyCBC [3–5] and GstLAL [6–8]. These analyses use a common set of template waveforms [9–11], but differ in their implementations of matched filtering [12,13], their use of detector data-quality information [14], the techniques used to mitigate the effect of non-Gaussian noise transients in the detector [6,15], and the methods for estimating the noise background of the search [4,16].

GW150914 was observed in both LIGO detectors [17] with a time-of-arrival difference of 7 ms, which is less than the 10 ms intersite propagation time, and a combined matched-filter signal-to-noise ratio (SNR) of 24. The search reported a false alarm rate estimated to be less than 1 event per 203000 years, equivalent to a significance greater than 5.1 σ. The basic features of the GW150914 signal point to it being produced by the coalescence of two black holes [1]. The best-fit template parameters from the search are consistent with detailed parameter estimation that identifies GW150914 as a near-equal mass black hole binary system with source-frame masses $36^{+5}_{-4}\,M_\odot$ and $29^{+4}_{-4}\,M_\odot$ at the 90% credible level [18].

The second most significant candidate event in the observation period (referred to as LVT151012) was reported on October 12, 2015, at 09:54:43 UTC with a combined matched-filter SNR of 9.6. The search reported a false alarm rate of 1 per 2.3 years and a corresponding false alarm probability of 0.02 for this candidate event. Detector characterization studies have not identified an instrumental or environmental artifact as causing this candidate event [14]. However, its false alarm probability is not sufficiently low to confidently claim this candidate event as a signal [19]. Detailed waveform analysis of this candidate event indicates that it is also a binary black hole merger with source frame masses $23^{+18}_{-6}\,M_\odot$ and $13^{+4}_{-5}\,M_\odot$, if it is of astrophysical origin.

This paper is organized as follows: Sec. II gives an overview of the compact binary coalescence search and the methods used. Sections III and IV describe the construction and tuning of the two independently implemented analyses used in the search. Section V presents the results of the search, and follow-up of the two most significant candidate events, GW150914 and LVT151012.

II. SEARCH DESCRIPTION

The binary coalescence search [20–27] reported here targets gravitational waves from binary neutron stars, binary black holes, and neutron star–black hole binaries, using matched filtering [28] with waveforms predicted by general relativity. Both the PyCBC and GstLAL analyses correlate the detector data with template waveforms that model the expected signal. The analyses identify candidate events that are detected at both observatories consistent

[*]Full author list given at the end of the article.

with the 10 ms intersite propagation time. Events are assigned a detection-statistic value that ranks their likelihood of being a gravitational-wave signal. This detection statistic is compared to the estimated detector noise background to determine the probability that a candidate event is due to detector noise.

We report on a search using coincident observations between the two Advanced LIGO detectors [29] in Hanford, Washington (H1), and in Livingston, Louisiana (L1), from September 12 to October 20, 2015. During these 38.6 days, the detectors were in coincident operation for a total of 18.4 days. Unstable instrumental operation and hardware failures affected 20.7 hours of these coincident observations. These data are discarded and the remaining 17.5 days are used as input to the analyses [14]. The analyses reduce this time further by imposing a minimum length over which the detectors must be operating stably; this is different between the two analyses (2064 s for PyCBC and 512 s for GstLAL), as described in Secs. III and IV. After applying this cut, the PyCBC analysis searched 16 days of coincident data and the GstLAL analysis searched 17 days of coincident data. To prevent bias in the results, the configuration and tuning of the analyses were determined using data taken prior to September 12, 2015.

A gravitational-wave signal incident on an interferometer alters its arm lengths by δL_x and δL_y, such that their measured difference is $\Delta L(t) = \delta L_x - \delta L_y = h(t)L$, where $h(t)$ is the gravitational-wave metric perturbation projected onto the detector, and L is the unperturbed arm length [30]. The strain is calibrated by measuring the detector's response to test mass motion induced by photon pressure from a modulated calibration laser beam [31]. Changes in the detector's thermal and alignment state cause small, time-dependent systematic errors in the calibration [31]. The calibration used for this search does not include these time-dependent factors. Appendix A demonstrates that neglecting the time-dependent calibration factors does not affect the result of this search.

The gravitational waveform $h(t)$ depends on the chirp mass of the binary, $\mathcal{M} = (m_1 m_2)^{3/5}/(m_1 + m_2)^{1/5}$ [32,33]; the symmetric mass ratio $\eta = (m_1 m_2)/(m_1 + m_2)^2$ [34]; and the angular momentum of the compact objects $\chi_{1,2} = c\mathbf{S}_{1,2}/Gm_{1,2}^2$ [35,36] (the compact object's dimensionless spin), where $\mathbf{S}_{1,2}$ is the angular momentum of the compact objects. The effect of spin on the waveform depends also on the ratio between the component objects' masses [37]. Parameters which affect the overall amplitude and phase of the signal as observed in the detector are maximized over in the matched-filter search, but can be recovered through full parameter estimation analysis [18]. The search parameter space is therefore defined by the limits placed on the compact objects' masses and spins. The minimum component masses of the search are determined by the lowest expected neutron star mass, which we assume to be $1\,\mathrm{M}_\odot$ [38]. There is no known maximum black hole mass [39]; however we limit this search to binaries with a total mass less than $M = m_1 + m_2 \leq 100\,\mathrm{M}_\odot$. The LIGO detectors are sensitive to higher mass binaries, however; the results of searches for binaries that lie outside this search space will be reported in future publications.

The limit on the spins of the compact objects $\chi_{1,2}$ are informed by radio and x-ray observations of compact-object binaries. The shortest observed pulsar period in a double neutron star system is 22 ms [40], corresponding to a spin of 0.02. Observations of x-ray binaries indicate that astrophysical black holes may have near extremal spins [41]. In constructing the search, we assume that compact objects with masses less than $2\,\mathrm{M}_\odot$ are neutron stars and we limit the magnitude of the component object's spin to $0 \leq \chi \leq 0.05$. For higher masses, the spin magnitude is limited to $0 \leq \chi \leq 0.9895$, with the upper limit set by our ability to generate valid template waveforms at high spins [9]. At current detector sensitivity, limiting spins to $\chi_{1,2} \leq 0.05$ for $m_{1,2} \leq 2\,\mathrm{M}_\odot$ does not reduce the search sensitivity for sources containing neutron stars with spins up to 0.4, the spin of the fastest-spinning millisecond pulsar [42]. Figure 1 shows the boundaries of the search parameter space in the component-mass plane, with the boundaries on the mass-dependent spin limits indicated.

Since the parameters of signals are not known in advance, each detector's output is filtered against a discrete bank of templates that span the search target space [21,43–46]. The placement of templates depends on the shape of the power spectrum of the detector noise. Both analyses use a low-frequency cutoff of 30 Hz for the search. The average

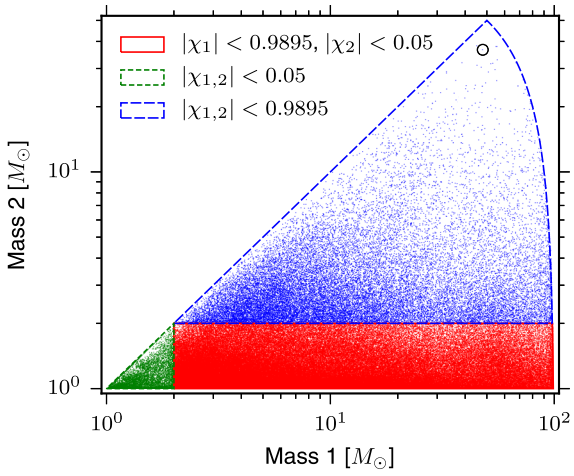

FIG. 1. The four-dimensional search parameter space covered by the template bank shown projected into the component-mass plane, using the convention $m_1 > m_2$. The lines bound mass regions with different limits on the dimensionless aligned-spin parameters χ_1 and χ_2. Each point indicates the position of a template in the bank. The circle highlights the template that best matches GW150914. This does not coincide with the best-fit parameters due to the discrete nature of the template bank.

noise power spectral density of the LIGO detectors was measured over the period of September 12 to September 26, 2015. The harmonic mean of these noise spectra from the two detectors was used to place a single template bank that was used for the duration of the search [4,47]. The templates are placed using a combination of geometric and stochastic methods [7,11,48,49] such that the loss in matched-filter SNR caused by its discrete nature is $\lesssim 3\%$. Approximately 250,000 template waveforms are used to cover this parameter space, as shown in Fig. 1.

The performance of the template bank is measured by the fitting factor [50]; this is the fraction of the maximum signal-to-noise ratio that can be recovered by the template bank for a signal that lies within the region covered by the bank. The fitting factor is measured numerically by simulating a signal and determining the maximum recovered matched-filter SNR over the template bank. Figure 2 shows the resulting distribution of fitting factors obtained for the template bank over the observation period. The loss in matched-filter SNR is less than 3% for more than 99% of the 10^5 simulated signals.

The template bank assumes that the spins of the two compact objects are aligned with the orbital angular momentum. The resulting templates can nonetheless effectively recover systems with misaligned spins in the parameter-space region of GW150914. To measure the effect of neglecting precession in the template waveforms, we compute the effective fitting factor which weights the fraction of the matched-filter SNR recovered by the amplitude of the signal [51]. When a signal with a poor orientation is projected onto the detector, the amplitude of the signal may be too small to detect even if there were no mismatch between the signal and the template; the weighting in the effective fitting accounts for this. Figure 3 shows the effective fitting factor for simulated signals from a population of simulated precessing binary black holes that are uniform in comoving volume [52,53]. The effective fitting factor is lowest at high mass ratios and low total mass, where the effects of precession are more pronounced. In the region close to the parameters of GW150914 the aligned-spin template bank is sensitive to a large fraction of precessing signals [53].

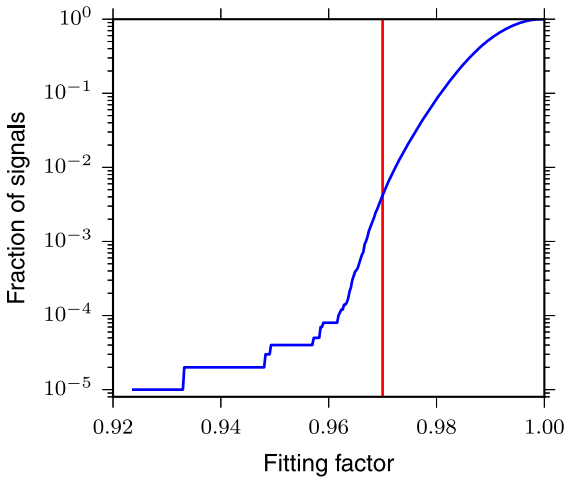

FIG. 2. Cumulative distribution of fitting factors obtained with the template bank for a population of simulated aligned-spin binary black hole signals. Less than 1% of the signals have a matched-filter SNR loss greater than 3%, demonstrating that the template bank has good coverage of the target search space.

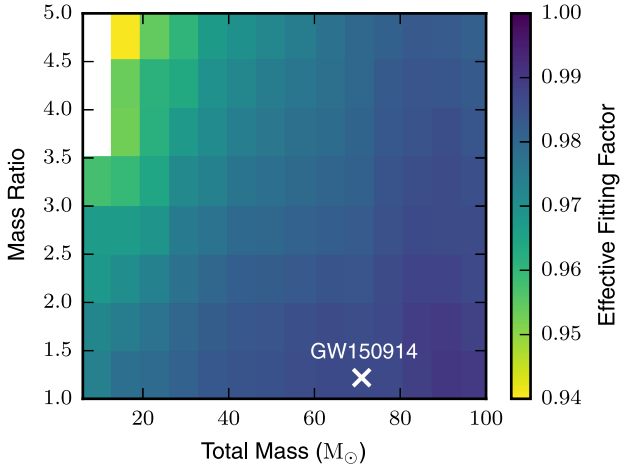

FIG. 3. The effective fitting factor between simulated precessing binary black hole signals and the template bank used for the search as a function of detector-frame total mass and mass ratio, averaged over each rectangular tile. The effective fitting factor gives the volume-averaged reduction in the sensitive distance of the search at fixed matched-filter SNR due to mismatch between the template bank and signals. The cross shows the location of GW150914. The high effective fitting factor near GW150914 demonstrates that the aligned-spin template bank used in this search can effectively recover systems with misaligned spins and similar masses to GW150914.

In addition to possible gravitational-wave signals, the detector strain contains a stationary noise background that primarily arises from photon shot noise at high frequencies and seismic noise at low frequencies. In the mid-frequency range, detector commissioning has not yet reached the point where test mass thermal noise dominates, and the noise at mid frequencies is poorly understood [14,17,54]. The detector strain data also exhibit nonstationarity and non-Gaussian noise transients that arise from a variety of instrumental or environmental mechanisms. The measured strain $s(t)$ is the sum of possible gravitational-wave signals $h(t)$ and the different types of detector noise $n(t)$.

To monitor environmental disturbances and their influence on the detectors, each observatory site is equipped with an array of sensors [55]. Auxiliary instrumental channels also record the interferometer's operating point and the state of the detector's control systems. Many noise transients have distinct signatures, visible in environmental or auxiliary data channels that are not sensitive to gravitational waves. When a noise source with known physical

coupling between these channels and the detector strain data is active, a data-quality veto is created that is used to exclude these data from the search [14]. In the GstLAL analysis, time intervals flagged by data quality vetoes are removed prior to the filtering. In the PyCBC analysis, these data quality vetoes are applied after filtering. A total of 2 hours is removed from the analysis by data quality vetoes. Despite these detector characterization investigations, the data still contain nonstationary and non-Gaussian noise which can affect the astrophysical sensitivity of the search. Both analyses implement methods to identify loud, short-duration noise transients and remove them from the strain data before filtering.

The PyCBC and GstLAL analyses calculate the matched-filter SNR for each template and each detector's data [12,56]. In the PyCBC analysis, sources with total mass less than $4\,M_\odot$ are modeled by computing the inspiral waveform accurate to third-and-a-half post-Newtonian order [34,57,58]. To model systems with total mass larger than $4\,M_\odot$, we use templates based on the effective-one-body (EOB) formalism [59], which combines results from the post-Newtonian approach [34,58] with results from black hole perturbation theory and numerical relativity [9,60] to model the complete inspiral, merger and ringdown waveform. The waveform models used assume that the spins of the merging objects are aligned with the orbital angular momentum. The GstLAL analysis uses the same waveform families, but the boundary between post-Newtonian and EOB models is set at $\mathcal{M} = 1.74\,M_\odot$. Both analyses identify maxima of the matched-filter SNR (triggers) over the signal time of arrival.

To suppress large SNR values caused by non-Gaussian detector noise, the two analyses calculate additional tests to quantify the agreement between the data and the template. The PyCBC analysis calculates a chi-squared statistic to test whether the data in several different frequency bands are consistent with the matching template [15]. The value of the chi-squared statistic is used to compute a reweighted SNR for each maxima. The GstLAL analysis computes a goodness-of-fit between the measured and expected SNR time series for each trigger. The matched-filter SNR and goodness-of-fit values for each trigger are used as parameters in the GstLAL ranking statistic.

Both analyses enforce coincidence between detectors by selecting trigger pairs that occur within a 15 ms window and come from the same template. The 15 ms window is determined by the 10 ms intersite propagation time plus 5 ms for uncertainty in arrival time of weak signals. The PyCBC analysis discards any triggers that occur during the time of data-quality vetoes prior to computing coincidence. The remaining coincident events are ranked based on the quadrature sum of the reweighted SNR from both detectors [4]. The GstLAL analysis ranks coincident events using a likelihood ratio that quantifies the probability that a particular set of coincident trigger parameters is due to a signal versus the probability of obtaining the same set of parameters from noise [6].

The significance of a candidate event is determined by the search background. This is the rate at which detector noise produces events with a detection-statistic value equal to or higher than the candidate event (the false alarm rate). Estimating this background is challenging for two reasons: the detector noise is nonstationary and non-Gaussian, so its properties must be empirically determined; and it is not possible to shield the detector from gravitational waves to directly measure a signal-free background. The specific procedure used to estimate the background is different for the two analyses.

To measure the significance of candidate events, the PyCBC analysis artificially shifts the timestamps of one detector's triggers by an offset that is large compared to the intersite propagation time, and a new set of coincident events is produced based on this time-shifted data set. For instrumental noise that is uncorrelated between detectors this is an effective way to estimate the background. To account for the search background noise varying across the target signal space, candidate and background events are divided into three search classes based on template length. To account for having searched multiple classes, the measured significance is decreased by a trials factor equal to the number of classes [61].

The GstLAL analysis measures the noise background using the distribution of triggers that are not coincident in time. To account for the search background noise varying across the target signal space, the analysis divides the template bank into 248 bins. Signals are assumed to be equally likely across all bins and it is assumed that noise triggers are equally likely to produce a given SNR and goodness-of-fit value in any of the templates within a single bin. The estimated probability density function for the likelihood statistic is marginalized over the template bins and used to compute the probability of obtaining a noise event with a likelihood value larger than that of a candidate event.

The results of the independent analyses are two separate lists of candidate events, with each candidate event assigned a false alarm probability and false alarm rate. These quantities are used to determine if a gravitational-wave signal is present in the search. Simulated signals are added to the input strain data to validate the analyses, as described in Appendix B.

III. PYCBC ANALYSIS

The PyCBC analysis [3–5] uses fundamentally the same methods [12,15,62–72] as those used to search for gravitational waves from compact binaries in the Initial LIGO and Virgo detector era [73–84], with the improvements described in Refs. [3,4]. In this section, we describe the configuration and tuning of the PyCBC analysis used in this search. To prevent bias in the search result, the

configuration of the analysis was determined using data taken prior to the observation period searched. When GW150914 was discovered by the low-latency transient searches [1], all tuning of the PyCBC analysis was frozen to ensure that the reported false alarm probabilities are unbiased. No information from the low-latency transient search is used in this analysis.

Of the 17.5 days of data that are used as input to the analysis, the PyCBC analysis discards times for which either of the LIGO detectors was in its observation state for less than 2064s; shorter intervals are considered to be unstable detector operation by this analysis and are removed from the observation time. After discarding time removed by data-quality vetoes and periods when detector operation is considered unstable the observation time remaining is 16 days.

For each template $h(t)$ and for the strain data from a single detector $s(t)$, the analysis calculates the square of the matched-filter SNR defined by [12]

$$\rho^2(t) \equiv \frac{1}{\langle h|h\rangle} |\langle s|h\rangle(t)|^2, \tag{1}$$

where the correlation is defined by

$$\langle s|h\rangle(t) = 4\int_0^\infty \frac{\tilde{s}(f)\tilde{h}^*(f)}{S_n(f)} e^{2\pi i f t} \mathrm{d}f, \tag{2}$$

where $\tilde{s}(f)$ is the Fourier transform of the time-domain quantity $s(t)$ given by

$$\tilde{s}(f) = \int_{-\infty}^{\infty} s(t) e^{-2\pi i f t} \mathrm{d}t. \tag{3}$$

The quantity $S_n(|f|)$ is the one-sided average power spectral density of the detector noise, which is recalculated every 2048s (in contrast to the fixed spectrum used in template bank construction). Calculation of the matched-filter SNR in the frequency domain allows the use of the computationally efficient fast Fourier transform [85,86]. The square of the matched-filter SNR in Eq. (1) is normalized by

$$\langle h|h\rangle = 4\int_0^\infty \frac{\tilde{h}(f)\tilde{h}^*(f)}{S_n(f)} \mathrm{d}f, \tag{4}$$

so that its mean value is 2, if $s(t)$ contains only stationary noise [87].

Non-Gaussian noise transients in the detector can produce extended periods of elevated matched-filter SNR that increase the search background [4]. To mitigate this, a time-frequency excess power (burst) search [88] is used to identify high-amplitude, short-duration transients that are not flagged by data-quality vetoes. If the burst search generates a trigger with a burst SNR exceeding 300, the PyCBC analysis vetoes these data by zeroing out 0.5s of $s(t)$ centered on the time of the trigger. The data are smoothly rolled off using a Tukey window during the 0.25 s before and after the vetoed data. The threshold of 300 is chosen to be significantly higher than the burst SNR obtained from plausible binary signals. For comparison, the burst SNR of GW150914 in the excess power search is ∼10. A total of 450 burst-transient vetoes is produced in the two detectors, resulting in 225 s of data removed from the search. A time-frequency spectrogram of the data at the time of each burst-transient veto was inspected to ensure that none of these windows contained the signature of an extremely loud binary coalescence.

The analysis places a threshold of 5.5 on the single-detector matched-filter SNR and identifies maxima of $\rho(t)$ with respect to the time of arrival of the signal. For each maximum we calculate a chi-squared statistic to determine whether the data in several different frequency bands are consistent with the matching template [15]. Given a specific number of frequency bands p, the value of the reduced chi-squared is given by

$$\chi_r^2 = \frac{p}{2p-2}\frac{1}{\langle h|h\rangle}\sum_{i=1}^{p}\left|\langle s|h_i\rangle - \frac{\langle s|h\rangle}{p}\right|^2, \tag{5}$$

where h_i is the subtemplate corresponding to the ith frequency band. Values of χ_r^2 near unity indicate that the signal is consistent with a coalescence. To suppress triggers from noise transients with large matched-filter SNR, $\rho(t)$ is reweighted by [64,82]

$$\hat{\rho} = \begin{cases} \rho/[(1+(\chi_r^2)^3)/2]^{\frac{1}{6}}, & \text{if } \chi_r^2 > 1, \\ \rho, & \text{if } \chi_r^2 \le 1. \end{cases} \tag{6}$$

Triggers that have a reweighted SNR $\hat{\rho} < 5$ or that occur during times subject to data-quality vetoes are discarded.

The template waveforms span a wide region of time-frequency parameter space and the susceptibility of the analysis to a particular type of noise transient can vary across the search space. This is demonstrated in Fig. 4 which shows the cumulative number of noise triggers as a function of reweighted SNR for Advanced LIGO engineering run data taken between September 2 and September 9, 2015. The response of the template bank to noise transients is well characterized by the gravitational-wave frequency at the template's peak amplitude, f_{peak}. Waveforms with a lower peak frequency have fewer cycles in the detector's most sensitive frequency band from 30–2000 Hz [17,54], and so are less easily distinguished from noise transients by the reweighted SNR.

The number of bins in the chi-squared test is a tunable parameter in the analysis [4]. Previous searches used a fixed number of bins [89] with the most recent Initial LIGO and Virgo searches using $p = 16$ bins for all templates [82,83]. Investigations on data from LIGO's sixth science run

[83,90] showed that better noise rejection is achieved with a template-dependent number of bins. The left two panels of Fig. 4 show the cumulative number of noise triggers with $p = 16$ bins used in the chi-squared test. Empirically, we find that choosing the number of bins according to

$$p = \lfloor 0.4(f_{\rm peak}/{\rm Hz})^{2/3} \rfloor \tag{7}$$

gives better suppression of noise transients in Advanced LIGO data, as shown in the right panels of Fig. 4.

The PyCBC analysis enforces signal coincidence between detectors by selecting trigger pairs that occur within a 15 ms window and come from the same template. We rank coincident events based on the quadrature sum $\hat{\rho}_c$ of the $\hat{\rho}$ from both detectors [4]. The final step of the analysis is to cluster the coincident events, by selecting those with the largest value of $\hat{\rho}_c$ in each time window of 10 s. Any other events in the same time window are discarded. This ensures that a loud signal or transient noise artifact gives rise to at most one candidate event [4].

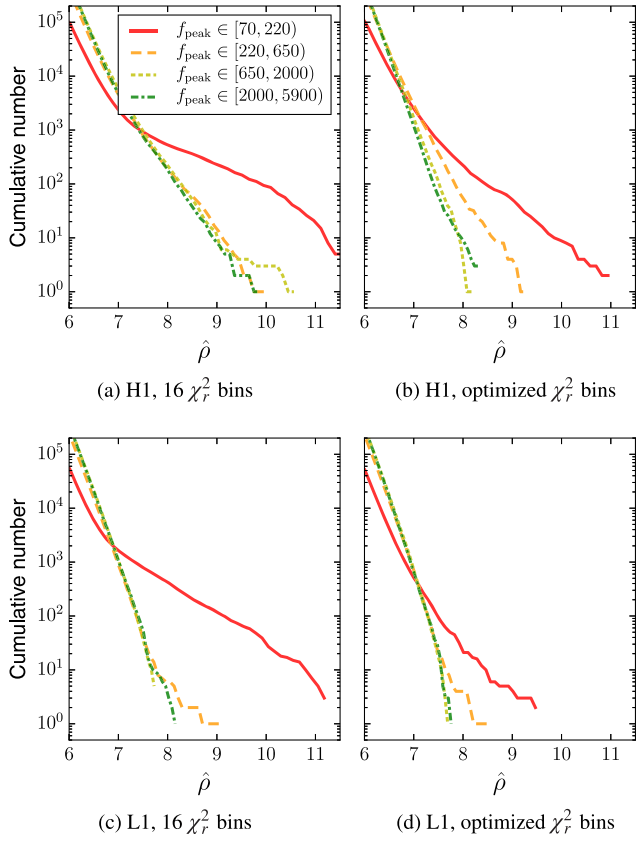

(a) H1, 16 χ^2_r bins (b) H1, optimized χ^2_r bins

(c) L1, 16 χ^2_r bins (d) L1, optimized χ^2_r bins

FIG. 4. Distributions of noise triggers over reweighted SNR $\hat{\rho}$, for Advanced LIGO engineering run data taken between September 2 and September 9, 2015. Each line shows triggers from templates within a given range of gravitational-wave frequency at maximum strain amplitude, $f_{\rm peak}$. Left: Triggers obtained from H1, L1 data respectively, using a fixed number of $p = 16$ frequency bands for the chi-squared test. Right: Triggers obtained with the number of frequency bands determined by the function $p = \lfloor 0.4(f_{\rm peak}/{\rm Hz})^{2/3} \rfloor$. Note that while noise distributions are suppressed over the whole template bank with the optimized choice of p, the suppression is strongest for templates with lower $f_{\rm peak}$ values. Templates that have a $f_{\rm peak} < 220$ Hz produce a large tail of noise triggers with high reweighted SNR even with the improved chi-squared test tuning; thus we separate these templates from the rest of the bank when calculating the noise background.

The significance of a candidate event is determined by the rate at which detector noise produces events with a detection-statistic value equal to or higher than that of the candidate event. To measure this, the analysis creates a "background data set" by artificially shifting the time-stamps of one detector's triggers by many multiples of 0.1 s and computing a new set of coincident events. Since the time offset used is always larger than the time-coincidence window, coincident signals do not contribute to this background. Under the assumption that noise is not correlated between the detectors [14], this method provides an unbiased estimate of the noise background of the analysis.

To account for the noise background varying across the target signal space, candidate and background events are divided into different search classes based on template length. Based on empirical tuning using Advanced LIGO engineering run data taken between September 2 and September 9, 2015, we divide the template space into three classes according to (i) $\mathcal{M} < 1.74\,{\rm M}_\odot$, (ii) $\mathcal{M} \geq 1.74\,{\rm M}_\odot$ and $f_{\rm peak} \geq 220$ Hz, and (iii) $\mathcal{M} \geq 1.74\,{\rm M}_\odot$ and $f_{\rm peak} < 220$ Hz. The significance of candidate events is measured against the background from the same class. For each candidate event, we compute the false alarm probability $\mathcal{F}$. This is the probability of finding one or more noise background events in the observation time with a detection-statistic value above that of the candidate event, given by [4,91]

$$\begin{aligned}\mathcal{F}(\hat{\rho}_c) &\equiv P(\geq 1 \text{ noise event above } \hat{\rho}_c | T, T_b) \\ &= 1 - \exp\left[-T\frac{1 + n_b(\hat{\rho}_c)}{T_b}\right],\end{aligned} \tag{8}$$

where T is the observation time of the search, T_b is the background time, and $n_b(\hat{\rho}_c)$ is the number of noise background triggers above the candidate event's reweighted SNR $\hat{\rho}_c$.

Equation (8) is derived assuming Poisson statistics for the counts of time-shifted background events, and for the count of coincident noise events in the search [4,91]. This assumption requires that different time-shifted analyses (i.e. with different relative shifts between detectors) give independent realizations of a counting experiment for noise background events. We expect different time shifts to yield independent event counts since the 0.1 s offset time is greater than the 10 ms gravitational-wave travel time between the sites plus the ∼1 ms autocorrelation length of the templates. To test the independence of event counts over different time shifts over this observation

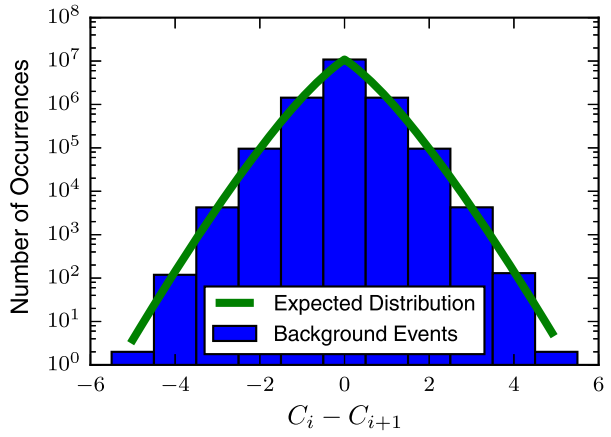

FIG. 5. The distribution of the differences in the number of events between consecutive time shifts, where C_i denotes the number of events in the ith time shift. The green line shows the predicted distribution for independent Poisson processes with means equal to the average event rate per time shift. The blue histogram shows the distribution obtained from time-shifted analyses. The variance of the time-shifted background distribution is 1.996, consistent with the predicted variance of 2. The distribution of background event counts in adjacent time shifts is well modeled by independent Poisson processes.

period, we compute the differences in the number of background events having $\hat{\rho}_c > 9$ between consecutive time shifts. Figure 5 shows that the measured differences on these data follow the expected distribution for the difference between two independent Poisson random variables [92], confirming the independence of time-shifted event counts.

If a candidate event's detection-statistic value is larger than that of any noise background event, as is the case for GW150914, then the PyCBC analysis places an upper bound on the candidate's false alarm probability. After discarding time removed by data-quality vetoes and periods when the detector is in stable operation for less than 2064 seconds, the total observation time remaining is $T = 16$ days. Repeating the time-shift procedure $\sim 10^7$ times on these data produces a noise background analysis time equivalent to $T_b = 608000$ years. Thus, the smallest false alarm probability that can be estimated in this analysis is approximately $\mathcal{F} = 7 \times 10^{-8}$. Since we treat the search parameter space as three independent classes, each of which may generate a false positive result, this value should be multiplied by a trials factor or look-elsewhere effect [61] of 3, resulting in a minimum measurable false alarm probability of $\mathcal{F} = 2 \times 10^{-7}$. The results of the PyCBC analysis are described in Sec. V.

IV. GSTLAL ANALYSIS

The GstLAL [93] analysis implements a time-domain matched-filter search [6] using techniques that were developed to perform the near real-time compact-object binary searches [7,8]. To accomplish this, the data $s(t)$ and templates $h(t)$ are each whitened in the frequency domain by dividing them by an estimate of the power spectral density of the detector noise. An estimate of the stationary noise amplitude spectrum is obtained with a combined median–geometric-mean modification of Welch's method [8]. This procedure is applied piecewise on overlapping Hann-windowed time-domain blocks that are subsequently summed together to yield a continuous whitened time series $s_w(t)$. The time-domain whitened template $h_w(t)$ is then convolved with the whitened data $s_w(t)$ to obtain the matched-filter SNR time series $\rho(t)$ for each template. By the convolution theorem, $\rho(t)$ obtained in this manner is the same as the $\rho(t)$ obtained by the frequency domain filtering in Eq. (1).

Of the 17.5 days of data that are used as input to the analysis, the GstLAL analysis discards times for which either of the LIGO detectors is in its observation state for less than 512 s in duration. Shorter intervals are considered to be unstable detector operation by this analysis and are removed from the observation time. After discarding time removed by data-quality vetoes and periods when the detector operation is considered unstable the observation time remaining is 17 days. To remove loud, short-duration noise transients, any excursions in the whitened data that are greater than 50σ are removed with 0.25 s padding. The intervals of $s_w(t)$ vetoed in this way are replaced with zeros. The cleaned whitened data are the input to the matched-filtering stage.

Adjacent waveforms in the template bank are highly correlated. The GstLAL analysis takes advantage of this to reduce the computational cost of the time-domain correlation. The templates are grouped by chirp mass and spin into 248 bins of ~1000 templates each. Within each bin, a reduced set of orthonormal basis functions $\hat{h}(t)$ is obtained via a singular value decomposition of the whitened templates. We find that the ratio of the number of orthonormal basis functions to the number of input waveforms is ~0.01–0.10, indicating a significant redundancy in each bin. The set of $\hat{h}(t)$ in each bin is convolved with the whitened data; linear combinations of the resulting time series are then used to reconstruct the matched-filter SNR time series for each template. This decomposition allows for computationally efficient time-domain filtering and reproduces the frequency-domain matched filter $\rho(t)$ to within 0.1% [6,56,94].

Peaks in the matched-filter SNR for each detector and each template are identified over 1 s windows. If the peak is above a matched-filter SNR of 4, it is recorded as a trigger. For each trigger, the matched-filter SNR time series around the trigger is checked for consistency with a signal by comparing the template's autocorrelation function $R(t)$ to the matched-filter SNR time series $\rho(t)$. The residual found after subtracting the autocorrelation function forms a goodness-of-fit test,

$$\xi^2 = \frac{1}{\mu}\int_{t_p-\delta t}^{t_p+\delta t} \mathrm{d}t|\rho(t_p)R(t) - \rho(t)|^2, \tag{9}$$

where t_p is the time at the peak matched-filter SNR $\rho(t_p)$, and δt is a tunable parameter. A suitable value for δt was found to be 85.45 ms (175 samples at a 2048 Hz sampling rate). The quantity μ normalizes ξ^2 such that a well-fit signal has a mean value of 1 in Gaussian noise [8]. The ξ^2 value is recorded with the trigger.

Each trigger is checked for time coincidence with triggers from the same template in the other detector. If two triggers occur from the same template within 15 ms in both detectors, a coincident event is recorded. Coincident events are ranked according to a multidimensional likelihood ratio $\mathcal{L}$ [16,95] and then clustered in a ± 4 s time window. The likelihood ratio ranks candidate events by the ratio of the probability of observing matched-filter SNR and ξ^2 from signals (h) versus obtaining the same parameters from noise (n). Since the orthonormal filter decomposition already groups templates into regions with high overlap, we expect templates in each group to respond similarly to noise. We use the template group θ_i as an additional parameter in the likelihood ratio to account for how different regions of the compact binary parameter space are affected differently by noise processes. The likelihood ratio is thus

$$\mathcal{L} = \frac{p(\mathbf{x}_\mathrm{H}, \mathbf{x}_\mathrm{L}, D_\mathrm{H}, D_\mathrm{L}|\theta_i, \mathrm{h})}{p(\mathbf{x}_\mathrm{H}|\theta_i, \mathrm{n})p(\mathbf{x}_\mathrm{L}|\theta_i, \mathrm{n})}, \tag{10}$$

where $\mathbf{x}_d = \{\rho_d, {\xi^2}_d\}$ are the matched-filter SNR and ξ^2 in each detector, and D is a parameter that measures the distance sensitivity of the given detector during the time of a trigger.

The numerator of the likelihood ratio is generated using an astrophysical model of signals distributed isotropically in the nearby Universe to calculate the joint SNR distribution in the two detectors [16]. The ξ^2 distribution for the signal hypothesis assumes that the signal agrees to within $\sim$90% of the template waveform and that the nearby noise is Gaussian. We assume that all θ_i are equally likely for signals.

The noise is assumed to be uncorrelated between detectors. The denominator of the likelihood ratio therefore factors into the product of the distribution of noise triggers in each detector, $p(\mathbf{x}_d|\theta_i, \mathrm{n})$. We estimate these using a two-dimensional kernel density estimation [96] constructed from all of the single-detector triggers not found in coincidence in a single bin.

The likelihood ratio $\mathcal{L}$ provides a ranking of events such that larger values of $\mathcal{L}$ are associated with a higher probability of the data containing a signal. The likelihood ratio itself is not the probability that an event is a signal, nor does it give the probability that an event was caused by noise. Computing the probability that an event is a signal requires additional prior assumptions. Instead, for each candidate event, we compute the false alarm probability $\mathcal{F}$. This is the probability of finding one or more noise background events with a likelihood-ratio value greater than or equal to that of the candidate event. Assuming Poisson statistics for the background, this is given by

$$\mathcal{F}(\mathcal{L}) \equiv P(\mathcal{L}|T, \mathrm{n}) = 1 - \exp[-\lambda(\mathcal{L}|T, \mathrm{n})]. \tag{11}$$

Instead of using time shifts, the GstLAL analysis estimates the Poisson rate of background events $\lambda(\mathcal{L}|T, \mathrm{n})$ as

$$\lambda(\mathcal{L}|T, \mathrm{n}) = M(T)P(\mathcal{L}|\mathrm{n}), \tag{12}$$

where $M(T)$ is the number of coincident events found above threshold in the analysis time T, and $P(\mathcal{L}|\mathrm{n})$ is the probability of obtaining one or more events from noise with a likelihood ratio $\geq \mathcal{L}$ (the survival function). We find this by estimating the survival function in each template bin and then marginalize over the bins; i.e., $P(\mathcal{L}|\mathrm{n}) = \sum_i P(\mathcal{L}|\theta_i, \mathrm{n})P(\theta_i|\mathrm{n})$. In a single bin, the survival function is

$$P(\mathcal{L}|\theta_i, \mathrm{n}) = 1 - \int_{S(\mathcal{L})} p'(\mathbf{x}_\mathrm{H}|\theta_i, \mathrm{n})p'(\mathbf{x}_\mathrm{L}|\theta_i, \mathrm{n})\mathrm{d}\mathbf{x}_\mathrm{H}\mathrm{d}\mathbf{x}_\mathrm{L}. \tag{13}$$

Here, $p'(\mathbf{x}_d|\theta_i, \mathrm{n})$ are estimates of the distribution of triggers in each detector including all of the single-detector triggers, whereas the estimate of $p(\mathbf{x}_d|\theta_i, \mathrm{n})$ includes only those triggers which were not coincident. This is consistent with the assumption that the false alarm probability is computed assuming all events are noise.

The integration region $S(\mathcal{L})$ is the volume of the four-dimensional space of $\mathbf{x}_d$ for which the likelihood ratios are less than $\mathcal{L}$. We find this by Monte Carlo integration of our estimates of the single-detector noise distributions $p'(\mathbf{x}_d|\theta_i, \mathrm{n})$. This is approximately equal to the number of coincidences that can be formed from the single-detector triggers with likelihood ratios $\geq \mathcal{L}$ divided by the total number of possible coincidences. We therefore reach a minimum possible estimate of the survival function, without extrapolation, at the $\mathcal{L}$ for which $p'(\mathbf{x}_\mathrm{H}|\theta_i, \mathrm{n})p'(\mathbf{x}_\mathrm{L}|\theta_i, \mathrm{n}) \sim 1/N_\mathrm{H}(\theta_i)N_\mathrm{L}(\theta_i)$, where $N_d(\theta_i)$ are the total number of triggers in each detector in the ith bin.

GW150914 was more significant than any other combination of triggers. For that reason, we are interested in knowing the minimum false alarm probability that can be computed by the GstLAL analysis. All of the triggers in a template bin, regardless of the template from which they came, are used to construct the single-detector probability density distributions p' within that bin. The false alarm probability estimated by the GstLAL analysis is the probability that noise triggers occur within a ± 15 ms time window *and* occur in the same template. Under the assumption that triggers are uniformly distributed over

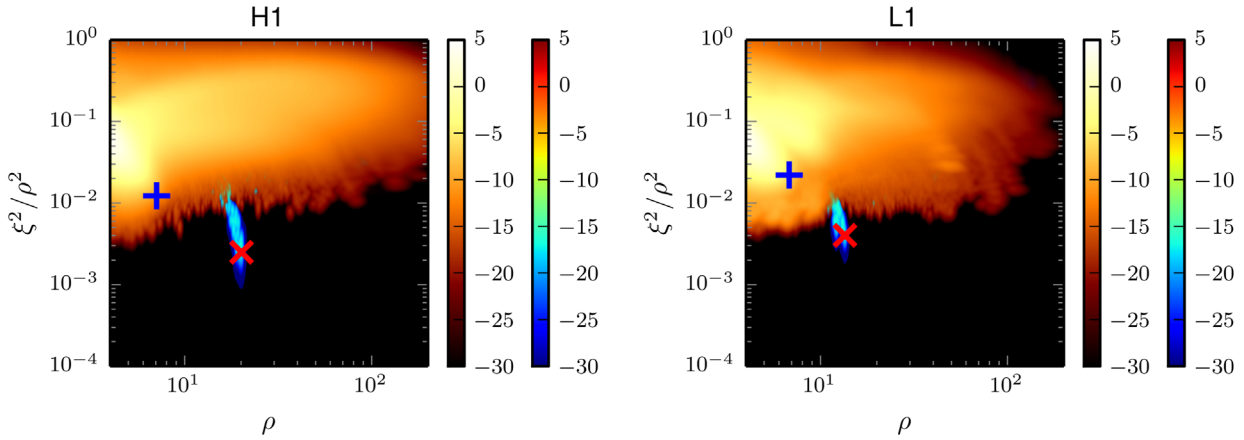

FIG. 6. Two projections of parameters in the multidimensional likelihood ratio ranking for GstLAL (left: H1, right: L1). The relative positions of GW150914 (red cross) and LVT151012 (blue plus) are indicated in the ξ^2/ρ^2 vs matched-filter SNR plane. The yellow-black colormap shows the natural logarithm of the probability density function calculated using only coincident triggers that are not coincident between the detectors. This is the background model used in the likelihood ratio calculation. The red-blue colormap shows the natural logarithm of the probability density function calculated from both coincident events and triggers that are not coincident between the detectors. The distribution showing both candidate events and noncoincident triggers has been masked to only show regions which are not consistent with the background model. Rather than showing the θ_i bins in which GW150914 and LVT151012 were found, θ_i has been marginalized over to demonstrate that no background triggers from any bin had the parameters of GW150914.

the bins, the minimum possible false alarm probability that can be computed is $MN_{\rm bins}/(N_{\rm H}N_{\rm L})$, where $N_{\rm bins}$ is the number of bins used, $N_{\rm H}$ is the total number of triggers in H, and $N_{\rm L}$ is the total number of triggers in L. For the present analysis, $M \sim 1 \times 10^9$, $N_{\rm H} \sim N_{\rm L} \sim 1 \times 10^{11}$, and $N_{\rm bins}$ is 248, yielding a minimum value of the false alarm probability of $\sim 10^{-11}$.

We cannot rule out the possibility that noise produced by the detectors violates the assumption that it is uniformly distributed among the templates within a bin. If we consider a more conservative noise hypothesis that does not assume that triggers are uniformly distributed within a bin and instead considers each template as a separate θ_i bin, we can evaluate the minimum upper bound on the false alarm probability of GW150914. This assumption would produce a larger minimum false alarm probability value by approximately the ratio of the number of templates to the present number of bins. Under this noise hypothesis, the minimum value of the false alarm probability would be $\sim 10^{-8}$, which is consistent with the minimum false alarm probability bound of the PyCBC analysis.

Figure 6 shows $p(\mathbf{x}_{\rm H}|{\rm n})$ and $p(\mathbf{x}_{\rm L}|{\rm n})$ in the warm colormap. The cool colormap includes triggers that are also found in coincidence, i.e., $p'(\mathbf{x}_{\rm H}|{\rm n})$ and $p'(\mathbf{x}_{\rm L}|{\rm n})$, which is the probability density function used to estimate $P(\mathcal{L}|{\rm n})$. It has been masked to only show regions which are not consistent with $p(\mathbf{x}_{\rm H}|{\rm n})$ and $p(\mathbf{x}_{\rm L}|{\rm n})$. In both cases θ_i has been marginalized over in order to show all the data on a single figure. The positions of the two loudest events, described in the next section, are shown. Figure 6 shows that GW150914 falls in a region without any noncoincident triggers from any bin.

V. SEARCH RESULTS

GW150914 was observed on September 14, 2015, at 09:50:45 UTC as the most significant event by both analyses. The individual detector triggers from GW150914 occurred within the 10 ms intersite propagation time with a combined matched-filter SNR of 24. Both pipelines report the same matched-filter SNR for the individual detector triggers in the Hanford detector ($\rho_{\rm H1} = 20$) and the Livingston detector ($\rho_{\rm L1} = 13$). GW150914 was found with the same template in both analyses with component masses $47.9\,{\rm M}_\odot$ and $36.6\,{\rm M}_\odot$. The effective spin of the best-matching template is $\chi_{\rm eff} = (c/G)(\mathbf{S_1}/m_1 + \mathbf{S_2}/m_2)\cdot(\hat{\mathbf{L}}/M) = 0.2$, where $\mathbf{S_{1,2}}$ are the spins of the compact objects and $\hat{\mathbf{L}}$ is the direction of the binary's orbital angular momentum. Due to the discrete nature of the template bank, follow-up parameter estimation is required to accurately determine the best-fit masses and spins of the binary's components [18,97].

The frequency at peak amplitude of the best-matching template is $f_{\rm peak} = 144$ Hz, placing it in noise-background class (iii) of the PyCBC analysis. Figure 7 (left) shows the result of the PyCBC analysis for this search class. In the time-shift analysis used to create the noise background estimate for the PyCBC analysis, a signal may contribute events to the background through random coincidences of the signal in one detector with noise in the other detector [91]. This can be seen in the background histogram shown by the black line. The tail is due to coincidence between the single-detector triggers from GW150914 and noise in the other detector. If a loud signal is in fact present, these random time-shifted coincidences contribute to an overestimate of the noise background and a more conservative

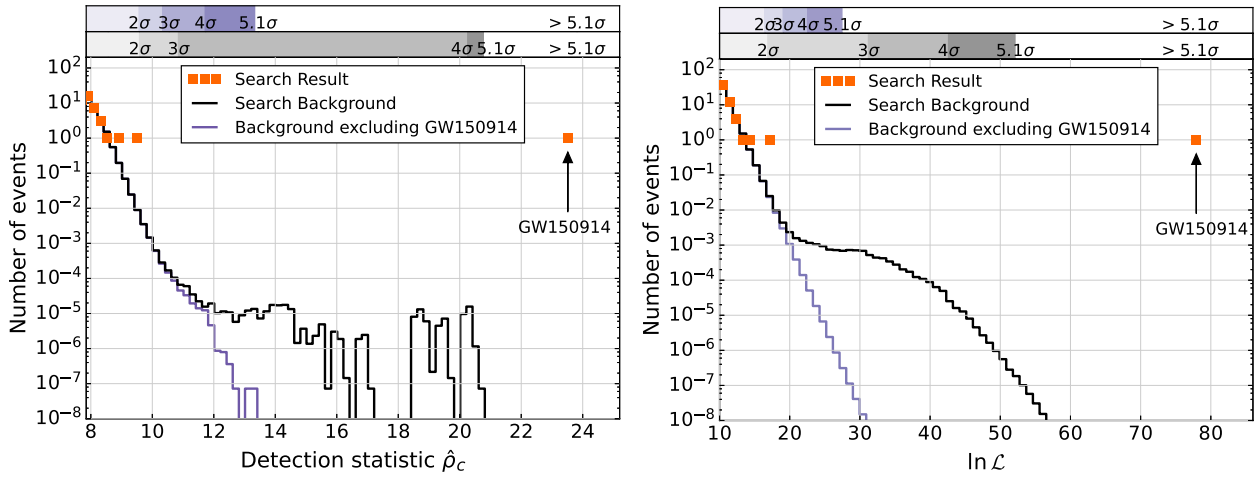

FIG. 7. Left: Search results from the PyCBC analysis. The histogram shows the number of candidate events (orange) and the number of background events due to noise in the search class where GW150914 was found (black) as a function of the search detection statistic and with a bin width of $\Delta\hat{\rho}_c = 0.2$. The significance of GW150914 is greater than 5.1 σ. The scales immediately above the histogram give the significance of an event measured against the noise backgrounds in units of Gaussian standard deviations as a function of the detection statistic. The black background histogram shows the result of the time-shift method to estimate the noise background in the observation period. The tail in the black-line background of the binary coalescence search is due to random coincidences of GW150914 in one detector with noise in the other detector. The significance of GW150914 is measured against the upper gray scale. The purple background histogram is the background excluding coincidences involving GW150914 and it is the background to be used to assess the significance of the second loudest event; the significance of this event is measured against the upper purple scale. Right: Search results from the GstLAL analysis. The histogram shows the observed candidate events (orange) as a function of the detection statistic ln $\mathcal{L}$. The black line indicates the expected background from noise where candidate events have been included in the noise background probability density function. The purple line indicates the expected background from noise where candidate events have not been included in the noise background probability density function. The independently implemented search methods and different background estimation method confirm the discovery of GW150914.

assessment of the significance of an event. Figure 7 (left) shows that GW150914 has a reweighted SNR $\hat{\rho}_c = 23.6$, greater than all background events in its class. This value is also greater than all background in the other two classes. As a result, we can only place an upper bound on the false alarm rate, as described in Sec. III. This bound is equal to the number of classes divided by the background time T_b. With three classes and $T_b = 608000$ years, we find the false alarm rate of GW150914 to be less than 5×10^{-6} yr^{-1}. With an observing time of 384 hr, the false alarm probability is $\mathcal{F} < 2 \times 10^{-7}$. Converting this false alarm probability to single-sided Gaussian standard deviations according to $-\sqrt{2}\mathrm{erf}^{-1}[1 - 2(1 - \mathcal{F})]$, where erf^{-1} is the inverse error function, the PyCBC analysis measures the significance of GW150914 as greater than 5.1 σ.

The GstLAL analysis reported a detection-statistic value for GW150914 of ln $\mathcal{L} = 78$, as shown in the right panel of Fig. 7. The GstLAL analysis estimates the false alarm probability assuming that noise triggers are equally likely to occur in any of the templates within a background bin. However, as stated in Sec. IV, if the distribution of noise triggers is not uniform across templates, particularly in the part of the bank where GW150914 is observed, the minimum false alarm probability would be higher. For this reason we quote the more conservative PyCBC bound on the false alarm probability of GW150914 here and in Ref. [1]. However, proceeding under the assumption that the noise triggers are equally likely to occur in any of the templates within a background bin, the GstLAL analysis estimates the false alarm probability of GW150914 to be 1.4×10^{-11}. The significance of GW150914 measured by GstLAL is consistent with the bound placed by the PyCBC analysis and provides additional confidence in the discovery of the signal.

The difference in time of arrival between the Livingston and Hanford detectors from the individual triggers in the PyCBC analysis is 7.1 ms, consistent with the time delay of $6.9^{+0.5}_{-0.4}$ ms recovered by parameter estimation [18]. Figure 8 (left) shows the matched-filter SNR ρ, the χ^2_r-statistic, and the reweighted SNR $\hat{\rho}$ for the best-matching template over a period of ± 5 ms around the time of GW150914 (we take the PyCBC trigger time in L1 as a reference). The matched-filter SNR peaks in both detectors at the time of the event and the value of the reduced chi-squared statistic is $\chi^2_{\mathrm{H1}} = 1$ and $\chi^2_{\mathrm{L1}} = 0.7$ at the time of the event, indicating an excellent match between the template and the data. The reweighted SNRs of the individual detector triggers of $\hat{\rho}_{\mathrm{H1}} = 19.5$ and $\hat{\rho}_{\mathrm{L1}} = 13.3$ are larger than that of any other single-detector triggers in the analysis; therefore the significance measurement of 5.1σ set using the 0.1 s time shifts is a conservative bound on the false alarm probability of GW150914.

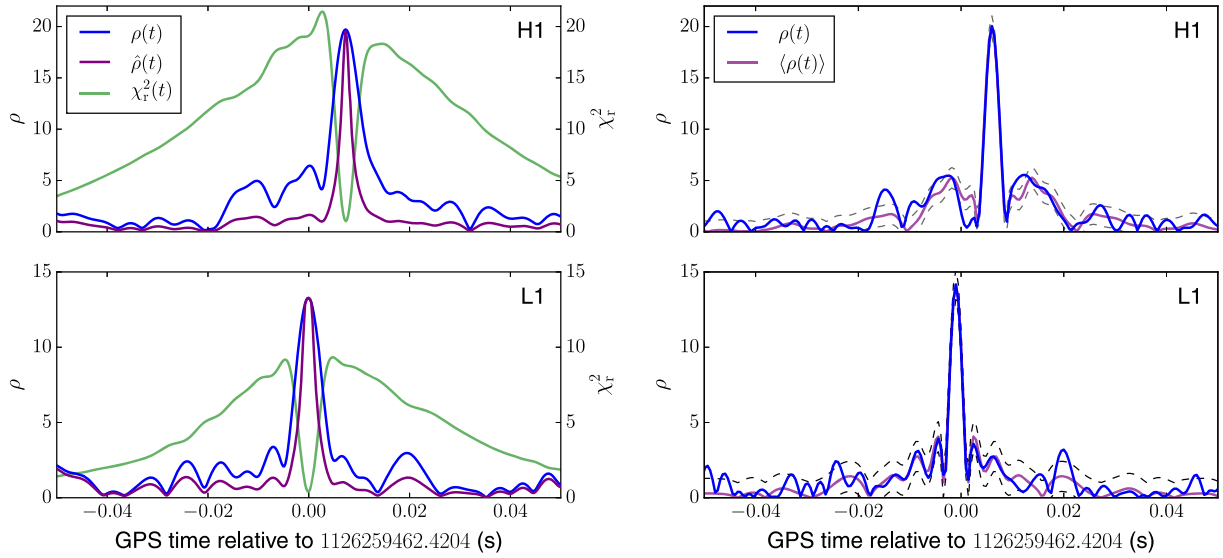

FIG. 8. Left: PyCBC matched-filter SNR (blue), reweighted SNR (purple) and χ^2_r (green) versus time of the best-matching template at the time of GW150914. The top plot shows the Hanford detector and the bottom, Livingston. Right: Observed matched-filter SNR (blue) and expected matched-filter SNR (purple) versus time for the best-matching template at the time of GW150914, as reported by the GstLAL analysis. The expected matched-filter SNR is based on the autocorrelation of the best-matching template. The dashed black lines indicate the 1σ deviations expected in Gaussian noise.

Figure 8 (right) shows ±5 ms of the GstLAL matched-filter SNR time series from each detector around the event time together with the predicted SNR time series computed from the autocorrelation function of the best-fit template. The difference between the autocorrelation and the observed matched-filter SNR is used to perform the GstLAL waveform-consistency test. The autocorrelation matches the observed matched-filter SNR extremely well, with consistency test values of $\xi_{\mathrm{H1}} = 1$ and $\xi_{\mathrm{L1}} = 0.7$. No other triggers with comparable matched-filter SNR had such low values of the signal-consistency test during the entire observation period.

Both analyses have shown that the probability that GW150914 was formed by random coincidence of detector noise is extremely small. We therefore conclude that GW150914 is a gravitational-wave signal. To measure the signal parameters, we use parameter estimation methods that assume the presence of a coherent coalescing binary signal in the data from both detectors [18,97]. Two waveform models were used which included inspiral, merger and ring-down portions of the signal: one which includes spin components aligned with orbital angular momentum [60,98] and one which includes the dominant modulation of the signal due to orbital precession caused by misaligned spins [99,100]. The parameter estimates are described by a continuous probability density function over the source parameters. We conclude that GW150914 is a nearly equal mass black hole binary system of source-frame masses $36^{+5}_{-4}\,\mathrm{M}_\odot$ and $29^{+4}_{-4}\,\mathrm{M}_\odot$ (median and 90% credible range). The spin magnitude of the primary black hole is constrained to be less than 0.7 with 90% probability. The most stringent constraint on the spins of the two black holes is on the effective spin parameter $\chi_{\mathrm{eff}} = -0.07^{+0.16}_{-0.17}$. The parameters of the best-fit template are consistent with these values, given the discrete nature of the template bank. We estimate GW150914 to be at a luminosity distance of 410^{+160}_{-180} Mpc, which corresponds to a redshift $0.09^{+0.03}_{-0.04}$. Full details of the source parameters for GW150914 are given in Ref. [18] and summarized in Table I.

TABLE I. Parameters of the two most significant events. The false alarm rate (FAR) and false alarm probability ($\mathcal{F}$) given here were determined by the PyCBC pipeline; the GstLAL results are consistent with this. The source-frame chirp mass $\mathcal{M}$, component masses $m_{1,2}$, effective spin χ_{eff}, and luminosity distance D_L are determined using a parameter estimation method that assumes the presence of a coherent compact binary coalescence signal starting at 20 Hz in the data [97]. The results are computed by averaging the posteriors for two model waveforms. Quoted uncertainties are 90% credible intervals that include statistical errors and systematic errors from averaging the results of different waveform models. Further parameter estimates of GW150914 are presented in Ref. [18].

Event	Time (UTC)	FAR (yr^{-1})	$\mathcal{F}$	$\mathcal{M}$ ($\mathrm{M}_\odot$)	m_1 ($\mathrm{M}_\odot$)	m_2 ($\mathrm{M}_\odot$)	χ_{eff}	D_L (Mpc)
GW150914	September 14, 2015, 09:50:45	$<5\times10^{-6}$	$<2\times10^{-7}$ ($>5.1\sigma$)	28^{+2}_{-2}	36^{+5}_{-4}	29^{+4}_{-4}	$-0.07^{+0.16}_{-0.17}$	410^{+160}_{-180}
LVT151012	October 12, 2015, 09:54:43	0.44	0.02 (2.1σ)	15^{+1}_{-1}	23^{+18}_{-6}	13^{+4}_{-5}	$0.0^{+0.3}_{-0.2}$	1100^{+500}_{-500}

When an event is confidently identified as a real gravitational wave signal, as for GW150914, the background used to determine the significance of other events is reestimated without the contribution of this event. This is the background distribution shown as purple lines in Fig. 7. Both analyses reported a candidate event on October 12, 2015, at 09:54:43 UTC as the second-loudest event in the observation period, which we refer to as LVT151012. This candidate event has a combined matched-filter SNR of 9.6. The PyCBC analysis reported a false alarm rate of 1 per 2.3 years and a corresponding false alarm probability of 0.02 for this event. The GstLAL analysis reported a false alarm rate of 1 per 1.1 years and a false alarm probability of 0.05. These results are consistent with expectations for candidate events with low matched-filter SNR, since PyCBC and GstLAL use different ranking statistics and background estimation methods. Detector characterization studies have not identified an instrumental or environmental artifact as causing this candidate event [14]; however its false alarm probability is not sufficiently low to confidently claim the event as a signal. It is significant enough to warrant follow-up, however. The results of signal parameter estimation, shown in Table I, indicate that if LVT151012 is of astrophysical origin, then the source would be a stellar-mass binary black hole system with source-frame component masses $23^{+18}_{-6}\,\mathrm{M}_{\odot}$ and $13^{+4}_{-5}\,\mathrm{M}_{\odot}$. The effective spin would be $\chi_{\mathrm{eff}} = 0.0^{+0.3}_{-0.2}$ and the distance 1100^{+500}_{-500} Mpc.

VI. CONCLUSION

The LIGO detectors have observed gravitational waves from the merger of two stellar-mass black holes. The binary coalescence search detects GW150914 with a significance greater than 5.1σ during the observations reported. This result is confirmed by two independent matched-filter analyses, providing confidence in the discovery. Detailed parameter estimation for GW150914 is reported in Ref. [18], the implications for the rate of binary black hole coalescences in Ref. [101], and tests for consistency of the signal with general relativity in Ref. [102]. Reference [103] discusses the astrophysical implications of this discovery. Full results of the compact binary search in Advanced LIGO's first observing run will be reported in a future publication.

ACKNOWLEDGMENTS

The authors gratefully acknowledge the support of the United States National Science Foundation (NSF) for the construction and operation of the LIGO Laboratory and Advanced LIGO as well as the Science and Technology Facilities Council (STFC) of the United Kingdom, the Max-Planck-Society (MPS), and the State of Niedersachsen/Germany for support of the construction of Advanced LIGO and construction and operation of the GEO 600 detector. Additional support for Advanced LIGO was provided by the Australian Research Council. The authors gratefully acknowledge the Italian Istituto Nazionale di Fisica Nucleare (INFN), the French Centre National de la Recherche Scientifique (CNRS) and the Foundation for Fundamental Research on Matter supported by the Netherlands Organisation for Scientific Research, for the construction and operation of the Virgo detector and the creation and support of the EGO consortium. The authors also gratefully acknowledge research support from these agencies as well as by the Council of Scientific and Industrial Research of India, Department of Science and Technology, India; Science & Engineering Research Board (SERB), India; Ministry of Human Resource Development, India; the Spanish Ministerio de Economía y Competitividad; the Conselleria d'Economia i Competitivitat and Conselleria d'Educació; Cultura i Universitats of the Govern de les Illes Balears; the National Science Centre of Poland; the European Commission; the Royal Society; the Scottish Funding Council; the Scottish Universities Physics Alliance; the Hungarian Scientific Research Fund (OTKA); the Lyon Institute of Origins (LIO); the National Research Foundation of Korea; Industry Canada and the Province of Ontario through the Ministry of Economic Development and Innovation; the National Science and Engineering Research Council Canada; Canadian Institute for Advanced Research; the Brazilian Ministry of Science, Technology, and Innovation; Russian Foundation for Basic Research; the Leverhulme Trust; the Research Corporation, Ministry of Science and Technology (MOST), Taiwan; and the Kavli Foundation. The authors gratefully acknowledge the support of the NSF, STFC, MPS, INFN, CNRS and the State of Niedersachsen/Germany for provision of computational resources.

APPENDIX A: DETECTOR CALIBRATION

The LIGO detectors do not directly record the strain signal; rather they sense power fluctuations in the light at the interferometer's readout port [29]. This error signal is used to generate a feedback signal to the detector's differential arm length to maintain destructive interference of the light moving towards the readout port [17]. The presence of this feedback signal suppresses the length change from external sources; a combination of the error and control signals is used to estimate the detector strain. The strain is calibrated by measuring the detector's response to test mass motion induced by photon pressure from a modulated calibration laser beam. Changes in the detector's thermal and alignment state cause small, time-dependent systematic errors in the calibration. For more details see Ref. [31].

Errors in the calibrated strain data lead to mismatches between waveform templates and the gravitational-wave signal. This mismatch has been shown to decrease the

expected SNR$\langle\rho\rangle$, but only has a weak, quadratic dependence on calibration errors [104,105]. However, the quantity used for detection is the reweighted SNR $\hat{\rho}(\rho,\chi_r^2)$ for each detector. In this appendix, we analyze the impact of calibration errors on $\hat{\rho}$ for signals similar to GW150914, and we find that the expected reweighted SNR$\langle\hat{\rho}\rangle$ also shows only a weak dependence on calibration errors.

In the frequency domain, the process of calibration reconstructs the gravitational-wave strain $h(f) = \Delta L(f)/L$ from the differential arm length error signal $d_{\rm err}(f)$, which is the filtered output of the photodiode. The function that relates the two quantities is the response function $R(f)$:

$$\Delta L(f) = R(f) d_{\rm err}(f). \tag{A1}$$

This response function is constructed from the sensing transfer function $C(f)$ that describes the frequency response of the detector to changes in the arm lengths as well as the actuation transfer function $A(f)$ that describes the motion of the test mass when driven by the control signal to maintain destructive interference in the interferometer [31].

The initial sensing and actuation transfer functions, measured before the start of the observing run, are defined by $C_0(f)$ and $A_0(f)$ respectively. However, over the course of an observing run, the frequency dependence of these transfer functions slowly drifts. The drift in the sensing function is parametrized by the real correction factor κ_C and the cavity pole frequency f_C, while the drift in the actuation function is parametrized by the complex correction factor for the actuation of the test mass κ_T as well as by the complex correction factor for the penultimate and upper-intermediate masses of the test-mass suspension system κ_{PU} [31]. This results in six real-time-dependent parameters, $\{\Re\kappa_T, \Im\kappa_T, \Re\kappa_{PU}, \Im\kappa_{PU}, \kappa_C, f_C\}$, with nominal values $\kappa_C = 1$, $\kappa_T = 1$, and $\kappa_{PU} = 1$ for the correction factors, as well as the cavity pole frequencies $f_C = 341$ Hz for H1 and $f_C = 388$ Hz for L1. The drift in these parameters is monitored by actuating the test masses at specific frequencies called calibration lines using the photon calibrator and electrostatic drive, and these parameters are found to deviate from their nominal values by no more than 10% [31].

The analysis for the discovery of GW150914 uses calibrated strain data that do not correct for these time varying parameters. We can evaluate the impact on $\hat{\rho}$ of not including these parameters by adding simulating signals to the strain data before filtering and adjusting these data with artificial values of these parameters. We performed software injections at 16 different times on September 14 and 15 using the best-match template for GW150914 given by the template waveform with parameters $m_1 = 47.9M_\odot$, $m_2 = 36.6M_\odot$, $\chi_1 = 0.962$, and $\chi_2 = -0.900$. We then vary each of the six time-dependent parameters and calculate $\hat{\rho}$ with PyCBC for the recalibrated strain.

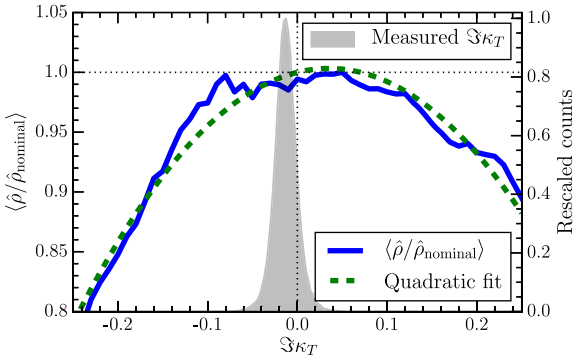

FIG. 9. Variation in $\hat{\rho}$ when the time-dependent parameter $\Im\kappa_T$ is adjusted. The solid blue curve represents $\hat{\rho}$ averaged over 16 software injections, with waveform parameters identical to the best-fit template for GW150914. $\hat{\rho}$ decreases as $\Im\kappa_T$ deviates from its nominal value. The green dashed curve is a quadratic fit, and represents the approximate behavior of $\langle\hat{\rho}\rangle$ if we had used a much larger number of software injections. The gray histogram represents the measured values of $\Im\kappa_T$ for times used in the analysis on September 14 and 15.

As an example, Fig. 9 shows the loss in $\hat{\rho}$ for H1 as the parameter $\Im\kappa_T$ is artificially adjusted from its nominal value of zero. Here, $\hat{\rho}$ is rescaled with respect to its value $\hat{\rho}_{\rm nominal}$ at $\Im\kappa_T = 0$ and then averaged over the 16 software injections to estimate $\langle\hat{\rho}/\hat{\rho}_{\rm nominal}\rangle$, the expected fractional loss in $\hat{\rho}$. For extreme values of $\Im\kappa_T$, the loss in $\hat{\rho}$ can be as much as ~20%. However, as shown by the histogram, the measured value of $\Im\kappa_T$ rarely deviates by more than 0.1 from its nominal value, leading to a loss in $\hat{\rho}$ of no more than 2%. The other five calibration parameters have a slightly smaller impact on $\hat{\rho}$. Similar results hold for L1, except for variations in $\Im\kappa_T$, which can lead to a loss in $\hat{\rho}$ of no more than 5%.

In addition to the dependence of $\langle\hat{\rho}\rangle$ on calibration errors presented in Fig. 9, individual realizations of $\hat{\rho}$ show an additional variation of approximately $\pm 2\%$ due to the power spectral density of the detector noise that is estimated from the strain data. For example, calibration errors affect the estimated noise power spectral density, and as a result, shift the bin boundaries used to calculate the χ_r^2 statistic. This subtle shift in the bin boundaries sometimes leads to a deviation in the measured value of $\hat{\rho}$ of about $\pm 2\%$ compared to its value if the bin boundaries had been fixed. The estimate of the noise power spectral density is also affected by the choice of start and end times for the 2048 s segments used to estimate the noise power spectral density, and this also affects $\hat{\rho}$ for GW150914 by approximately $\pm 2\%$. Overall, since the measured combined reweighted SNR $\hat{\rho}_c$ is significantly above the detection threshold, neglecting the time-variation of the calibration does not affect the result of this search.

APPENDIX B: ANALYSIS OF SIMULATED SIGNALS

Simulated signals are added to the detector data to validate the performance of our searches. These simulations can be added either in software, by adding a waveform to the input strain data, or by moving the detector's test masses in a way that simulates a gravitational-wave signal. Physically actuating on the detector's test masses provides a full end-to-end validation of our ability to detect signals at the expense of corrupting the data during the time of the simulated signal. Adding simulations in software allows us to repeat the analysis on the same data set many times, accumulating large statistics and testing search sensitivity across a large parameter space. Signals simulated in software have been used to constrain the coalescence rate of binary black hole systems in Ref. [101].

To validate the search, we generate a population of binary black holes with component masses between 2 and 98 $M_\odot$ and the full range of available spins using the template waveform. Signals are randomly distributed in sky location, orientation, distance, and time and then added coherently to each detector's strain data prior to filtering. The PyCBC and GstLAL analyses report the matched-filter SNR, and the χ_r^2 and ξ^2 statistics, respectively, for these simulated signals. In addition, we simulate eight signals in the detectors to test the recovery of GW150914. The signals were generated using the aligned-spin waveforms used in the search. The parameters were drawn from the posterior distribution of early GW150914 parameter estimation results. The sky positions of the signals were chosen to give similar amplitudes as GW150914 in the H1 and L1 detectors [18]. The signals are added to both detectors with the correct relative amplitude, phase, and time offsets to simulate a gravitational-wave signal from an astrophysical source.

Figure 10 shows the χ_r^2 and ξ^2 versus matched-filter SNR in each detector for a set of software-simulated binary black hole signals recovered by the PyCBC (top) and GstLAL (bottom) analyses. Also shown are the eight simulated signals that were physically added to the detector. The

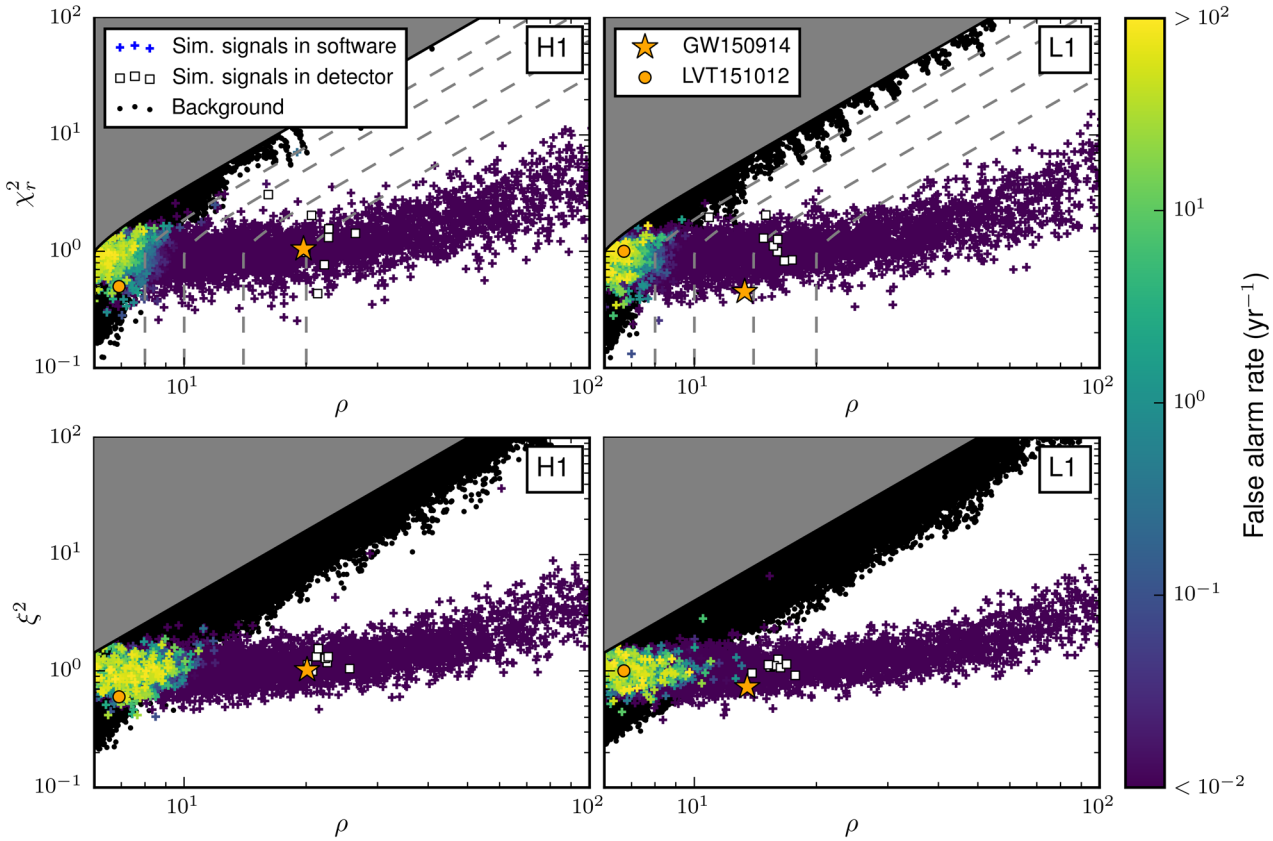

FIG. 10. PyCBC χ_r^2 (top row) and GstLAL ξ^2 (bottom row) versus SNR in each detector. Triggers associated with a set of simulated binary black hole signals that are added in software are shown, colored by the false alarm rate that they were recovered with (crosses). Also shown are triggers associated with simulated signals that were added to the detectors. We see a clear separation between these simulated signals and background noise triggers (black dots; for plotting purposes, a threshold was applied to the background, indicated by the gray region). Lines of constant reweighted SNR (gray dashed lines) are shown in the PyCBC plot; plotted are $\hat{\rho} = \{8, 10, 14, 20\}$.

parameters of GW150914 are shown with a star. We see a clear separation between signal and noise background in the region of GW150914 for both the software and physical (hardware) simulations. Simulated gravitational waves with similar parameters and distances as GW150914 are found with high significance by both analyses, validating the ability of the analyses described here to detect sources similar to GW150914.

[1] B. P. Abbott *et al.* (LIGO Scientific and Virgo Collaboration), Phys. Rev. Lett. **116**, 061102 (2016).
[2] B. P. Abbott *et al.* (LIGO Scientific and Virgo Collaboration), arXiv:1602.03843.
[3] T. Dal Canton *et al.*, Phys. Rev. D **90**, 082004 (2014).
[4] S. A. Usman *et al.*, arXiv:1508.02357.
[5] A. H. Nitz, I. W. Harry, J. L. Willis, C. M. Biwer, D. A. Brown, L. P. Pekowsky, T. Dal Canton, A. R. Williamson, T. Dent, C. D. Capano, T. T. Massinger, A. K. Lenon, A. Nielsen, and M. Cabero, PyCBC software, https://github.com/ligo-cbc/pycbc.
[6] K. Cannon, R. Cariou, A. Chapman, M. Crispin-Ortuzar, N. Fotopoulos *et al.*, Astrophys. J. **748**, 136 (2012).
[7] S. Privitera, S. R. P. Mohapatra, P. Ajith, K. Cannon, N. Fotopoulos, M. A. Frei, C. Hanna, A. J. Weinstein, and J. T. Whelan, Phys. Rev. D **89**, 024003 (2014).
[8] C. Messick *et al.*, arXiv:1604.04324.
[9] A. Taracchini, A. Buonanno, Y. Pan, T. Hinderer, M. Boyle *et al.*, Phys. Rev. D **89**, 061502 (2014).
[10] M. Pürrer, Phys. Rev. D **93**, 064041 (2016).
[11] C. Capano, I. Harry, S. Privitera, and A. Buonanno, arXiv:1602.03509.
[12] B. Allen, W. G. Anderson, P. R. Brady, D. A. Brown, and J. D. E. Creighton, Phys. Rev. D **85**, 122006 (2012).
[13] K. Cannon, A. Chapman, C. Hanna, D. Keppel, A. C. Searle, and A. J. Weinstein, Phys. Rev. D **82**, 044025 (2010).
[14] B. P. Abbott *et al.* (LIGO Scientific and Virgo Collaboration), arXiv:1602.03844.
[15] B. Allen, Phys. Rev. D **71**, 062001 (2005).
[16] K. Cannon, C. Hanna, and J. Peoples, arXiv:1504.04632.
[17] B. P. Abbott *et al.* (LIGO Scientific and Virgo Collaboration), Phys. Rev. Lett. **116**, 131103 (2016).
[18] B. P. Abbott *et al.* (LIGO Scientific and Virgo Collaboration), arXiv:1602.03840.
[19] G. Gonzàlez *et al.* (LIGO Scientific and Virgo Collaboration), https://dcc.ligo.org/LIGO-M1200055/public/main.
[20] K. S. Thorne, in *Three Hundred Years of Gravitation*, edited by S. W. Hawking and W. Israel (Cambridge University Press, Cambridge, 1987), Chap. 9, pp. 330–458.
[21] B. S. Sathyaprakash and S. V. Dhurandhar, Phys. Rev. D **44**, 3819 (1991).
[22] C. Cutler *et al.*, Phys. Rev. Lett. **70**, 2984 (1993).
[23] L. S. Finn, Phys. Rev. D **46**, 5236 (1992).
[24] L. S. Finn and D. F. Chernoff, Phys. Rev. D **47**, 2198 (1993).
[25] S. V. Dhurandhar and B. S. Sathyaprakash, Phys. Rev. D **49**, 1707 (1994).
[26] R. Balasubramanian, B. S. Sathyaprakash, and S. V. Dhurandhar, Phys. Rev. D **53**, 3033 (1996).
[27] E. E. Flanagan and S. A. Hughes, Phys. Rev. D **57**, 4535 (1998).
[28] L. A. Wainstein and V. D. Zubakov, *Extraction of Signals from Noise* (Prentice-Hall, Englewood Cliffs, NJ, 1962).
[29] J. Aasi *et al.* (LIGO Scientific Collaboration), Classical Quantum Gravity **32**, 115012 (2015).
[30] A. Abramovici *et al.*, Science **256**, 325 (1992).
[31] B. P. Abbott *et al.* (LIGO Scientific Collaboration), arXiv:1602.03845.
[32] P. C. Peters and J. Mathews, Phys. Rev. **131**, 435 (1963).
[33] P. C. Peters, Phys. Rev. **136**, B1224 (1964).
[34] L. Blanchet, T. Damour, B. R. Iyer, C. M. Will, and A. G. Wiseman, Phys. Rev. Lett. **74**, 3515 (1995).
[35] L. E. Kidder, C. M. Will, and A. G. Wiseman, Phys. Rev. D **47**, R4183 (1993).
[36] L. E. Kidder, Phys. Rev. D **52**, 821 (1995).
[37] L. Blanchet, Living Rev. Relativity **17**, 2 (2014).
[38] M. C. Miller and J. M. Miller, Phys. Rep. **548**, 1 (2015).
[39] K. Belczynski, A. Buonanno, M. Cantiello, C. L. Fryer, D. E. Holz, I. Mandel, M. C. Miller, and M. Walczak, Astrophys. J. **789**, 120 (2014).
[40] M. Burgay *et al.*, Nature (London) **426**, 531 (2003).
[41] J. E. McClintock, R. Narayan, and J. F. Steiner, Space Sci. Rev. **183**, 295 (2014).
[42] D. R. Lorimer, Living Rev. Relativity **11**, 8 (2008).
[43] B. J. Owen, Phys. Rev. D **53**, 6749 (1996).
[44] B. J. Owen and B. S. Sathyaprakash, Phys. Rev. D **60**, 022002 (1999).
[45] S. Babak, R. Balasubramanian, D. Churches, T. Cokelaer, and B. S. Sathyaprakash, Classical Quantum Gravity **23**, 5477 (2006).
[46] T. Cokelaer, Phys. Rev. D **76**, 102004 (2007).
[47] D. Keppel, arXiv:1307.4158.
[48] I. W. Harry, B. Allen, and B. Sathyaprakash, Phys. Rev. D **80**, 104014 (2009).
[49] D. A. Brown, I. Harry, A. Lundgren, and A. H. Nitz, Phys. Rev. D **86**, 084017 (2012).
[50] T. A. Apostolatos, Phys. Rev. D **54**, 2421 (1996).
[51] A. Buonanno, Y. Chen, and M. Vallisneri, Phys. Rev. D **67**, 104025 (2003); **74**, 029904(E) (2006).
[52] Y. Pan, A. Buonanno, A. Taracchini, L. E. Kidder, A. H. Mroué, H. P. Pfeiffer, M. A. Scheel, and B. Szilgyi, Phys. Rev. D **89**, 084006 (2014).
[53] I. Harry, S. Privitera, A. Bohe, and A. Buonanno, arXiv:1603.02444.
[54] D. Martynov *et al.*(LIGO Scientific), arXiv:1604.00439.

[55] A. Effler, R. M. S. Schofield, V. V. Frolov, G. Gonzalez, K. Kawabe, J. R. Smith, J. Birch, and R. McCarthy, Classical Quantum Gravity **32**, 035017 (2015).

[56] K. Cannon, A. Chapman, C. Hanna, D. Keppel, A. C. Searle, and A. J. Weinstein, Phys. Rev. D **82**, 044025 (2010).

[57] S. Droz, D. J. Knapp, E. Poisson, and B. J. Owen, Phys. Rev. D **59**, 124016 (1999).

[58] L. Blanchet, T. Damour, G. Esposito-Farèse, and B. R. Iyer, Phys. Rev. Lett. **93**, 091101 (2004).

[59] A. Buonanno and T. Damour, Phys. Rev. D **62**, 064015 (2000).

[60] M. Pürrer, Classical Quantum Gravity **31**, 195010 (2014).

[61] L. Lyons, Ann. Appl. Stat. **2**, 887 (2008).

[62] D. A. Brown *et al.*, Classical Quantum Gravity **21**, S1625 (2004).

[63] D. A. Brown (LIGO Scientific Collaboration), Classical Quantum Gravity **22**, S1097 (2005).

[64] S. Babak, R. Biswas, P. Brady, D. Brown, K. Cannon *et al.*, Phys. Rev. D **87**, 024033 (2013).

[65] D. A. Brown *et al.*, in *Workflows for e-Science*, edited by I. J. Taylor, E. Deelman, D. Gannon, and M. S. Shields (Springer-Verlag, Berlin, 2006), Chap. 5, pp. 41–61.

[66] E. Deelman, G. Singh, M.-H. Su, J. Blythe, Y. Gil, C. Kesselman, G. Mehta, K. Vahi, G. B. Berriman, J. Good, A. Laity, J. C. Jacob, and D. S. Katz, Scientific Programming Journal **13**, 219 (2005).

[67] E. Deelman, K. Vahi, G. Juve, M. Rynge, S. Callaghan, P. J. Maechling, R. Mayani, W. Chen, R. Ferreira da Silva, M. Livny, and K. Wenger, Future Gener. Comput. Syst. **46**, 17 (2015).

[68] D. Thain, T. Tannenbaum, and M. Livny, Concurrency and Computation: Practice and Experience **17**, 323 (2005).

[69] P. Couvares, T. Kosar, A. Roy, J. Weber, and K. Wenger, in *Workflows for e-Science*, edited by I. J. Taylor, E. Deelman, D. Gannon, and M. S. Shields (Springer, London, 2007), Chap. 22, pp. 357–375.

[70] E. Jones, T. Oliphant, P. Peterson *et al.*, SciPy: Open source scientific tools for Python, http://www.scipy.org/.

[71] S. v. d. Walt, S. C. Colbert, and G. Varoquaux, Comput. Sci. Eng. **13**, 22 (2011).

[72] J. D. Hunter, Comput. Sci. Eng. **9**, 90 (2007).

[73] B. Abbott *et al.* (LIGO Scientific Collaboration), Phys. Rev. D **69**, 122001 (2004).

[74] B. Abbott *et al.* (LIGO Scientific Collaboration), Phys. Rev. D **72**, 082001 (2005).

[75] B. Abbott *et al.* (LIGO Scientific Collaboration), Phys. Rev. D **72**, 082002 (2005).

[76] B. Abbott *et al.* (LIGO Scientific Collaboration), Phys. Rev. D **73**, 062001 (2006).

[77] B. Abbott *et al.* (LIGO Scientific Collaboration), Phys. Rev. D **77**, 062002 (2008).

[78] B. Abbott *et al.* (LIGO Scientific Collaboration), Phys. Rev. D **78**, 042002 (2008).

[79] B. Abbott *et al.* (LIGO Scientific Collaboration), Phys. Rev. D **79**, 122001 (2009).

[80] B. Abbott *et al.* (LIGO Scientific Collaboration), Phys. Rev. D **80**, 047101 (2009).

[81] J. Abadie *et al.* (LIGO Scientific Collaboration), Phys. Rev. D **82**, 102001 (2010).

[82] J. Abadie *et al.* (LIGO Scientific and Virgo Collaboration), Phys. Rev. D **85**, 082002 (2012).

[83] J. Aasi *et al.* (LIGO Scientific and Virgo Collaboration), Phys. Rev. D **87**, 022002 (2013).

[84] J. Aasi *et al.* (LIGO Scientific and Virgo Collaboration), Phys. Rev. D **89**, 102006 (2014).

[85] Intel Math Kernel Library, Intel Corporation, 2015.

[86] M. Frigo and S. G. Johnson, Proc. IEEE **93**, 216 (2005).

[87] C. Cutler and E. Flanagan, Phys. Rev. D **49**, 2658 (1994).

[88] F. Robinet, https://tds.ego-gw.it/ql/?c=10651.

[89] S. Babak, H. Grote, M. Hewitson, H. Luck, and K. A. Strain, Phys. Rev. D **72**, 022002 (2005).

[90] A. Nitz, Ph.D. thesis, Syracuse University, 2015.

[91] C. Capano, T. Dent, Y.-M. Hu, M. Hendry, C. Messenger, and J. Veitch, arXiv:1601.00130.

[92] J. G. Skellam, J. R. Stat. Soc. **109**, 296 (1946).

[93] https://wiki.ligo.org/DASWG/GstLAL.

[94] K. Cannon, C. Hanna, and D. Keppel, Phys. Rev. D **84**, 084003 (2011).

[95] K. C. Cannon, Classical Quantum Gravity **25**, 105024 (2008).

[96] B. W. Silverman, *Density Estimation for Statistics and Data Analysis* (Chapman & Hall, London, 1998).

[97] J. Veitch, V. Raymond, B. Farr, W. Farr, P. Graff *et al.*, Phys. Rev. D **91**, 042003 (2015).

[98] Y. Pan, A. Buonanno, L. T. Buchman, T. Chu, L. E. Kidder, H. P. Pfeiffer, and M. A. Scheel, Phys. Rev. D **81**, 084041 (2010).

[99] M. Hannam, P. Schmidt, A. Bohé, L. Haegel, S. Husa, F. Ohme, G. Pratten, and M. Pürrer, Phys. Rev. Lett. **113**, 151101 (2014).

[100] S. Khan, S. Husa, M. Hannam, F. Ohme, M. Prrer, X. J. Forteza, and A. Boh, Phys. Rev. D **93**, 044007 (2016).

[101] B. P. Abbott *et al.* (LIGO Scientific and Virgo Collaboration), arXiv:1602.03842.

[102] B. P. Abbott *et al.* (LIGO Scientific and Virgo Collaboration), arXiv:1602.03841.

[103] B. P. Abbott *et al.* (LIGO Scientific and Virgo Collaboration), Astrophys. J. **818**, L22 (2016).

[104] B. Allen, LIGO Calibration Accuracy, Tech. Rep. LIGO-T960189-00-Z, LIGO Project, 1996.

[105] D. A. Brown (LIGO Scientific Collaboration), Classical Quantum Gravity **21**, S797 (2004).

B. P. Abbott,[1] R. Abbott,[1] T. D. Abbott,[2] M. R. Abernathy,[1] F. Acernese,[3,4] K. Ackley,[5] C. Adams,[6] T. Adams,[7] P. Addesso,[3] R. X. Adhikari,[1] V. B. Adya,[8] C. Affeldt,[8] M. Agathos,[9] K. Agatsuma,[9] N. Aggarwal,[10] O. D. Aguiar,[11] L. Aiello,[12,13] A. Ain,[14] P. Ajith,[15] B. Allen,[8,16,17] A. Allocca,[18,19] P. A. Altin,[20] S. B. Anderson,[1] W. G. Anderson,[16] K. Arai,[1] M. C. Araya,[1]

C. C. Arceneaux,[21] J. S. Areeda,[22] N. Arnaud,[23] K. G. Arun,[24] S. Ascenzi,[25,13] G. Ashton,[26] M. Ast,[27] S. M. Aston,[6] P. Astone,[28] P. Aufmuth,[8] C. Aulbert,[8] S. Babak,[29] P. Bacon,[30] M. K. M. Bader,[9] P. T. Baker,[31] F. Baldaccini,[32,33] G. Ballardin,[34] S. W. Ballmer,[35] J. C. Barayoga,[1] S. E. Barclay,[36] B. C. Barish,[1] D. Barker,[37] F. Barone,[3,4] B. Barr,[36] L. Barsotti,[10] M. Barsuglia,[30] D. Barta,[38] J. Bartlett,[37] I. Bartos,[39] R. Bassiri,[40] A. Basti,[18,19] J. C. Batch,[37] C. Baune,[8] V. Bavigadda,[34] M. Bazzan,[41,42] B. Behnke,[29] M. Bejger,[43] A. S. Bell,[36] C. J. Bell,[36] B. K. Berger,[1] J. Bergman,[37] G. Bergmann,[8] C. P. L. Berry,[44] D. Bersanetti,[45,46] A. Bertolini,[9] J. Betzwieser,[6] S. Bhagwat,[35] R. Bhandare,[47] I. A. Bilenko,[48] G. Billingsley,[1] J. Birch,[6] R. Birney,[49] S. Biscans,[10] A. Bisht,[8,17] M. Bitossi,[34] C. Biwer,[35] M. A. Bizouard,[23] J. K. Blackburn,[1] C. D. Blair,[50] D. G. Blair,[50] R. M. Blair,[37] S. Bloemen,[51] O. Bock,[8] T. P. Bodiya,[10] M. Boer,[52] G. Bogaert,[52] C. Bogan,[8] A. Bohe,[29] K. Bohémier,[35] P. Bojtos,[53] C. Bond,[44] F. Bondu,[54] R. Bonnand,[7] B. A. Boom,[9] R. Bork,[1] V. Boschi,[18,19] S. Bose,[55,14] Y. Bouffanais,[30] A. Bozzi,[34] C. Bradaschia,[19] P. R. Brady,[16] V. B. Braginsky,[48] M. Branchesi,[56,57] J. E. Brau,[58] T. Briant,[59] A. Brillet,[52] M. Brinkmann,[8] V. Brisson,[23] P. Brockill,[16] A. F. Brooks,[1] D. A. Brown,[35] D. D. Brown,[44] N. M. Brown,[10] C. C. Buchanan,[2] A. Buikema,[10] T. Bulik,[60] H. J. Bulten,[61,9] A. Buonanno,[29,62] D. Buskulic,[7] C. Buy,[30] R. L. Byer,[40] M. Cabero,[8] L. Cadonati,[63] G. Cagnoli,[64,65] C. Cahillane,[1] J. Calderón Bustillo,[66,63] T. Callister,[1] E. Calloni,[67,4] J. B. Camp,[68] K. C. Cannon,[69] J. Cao,[70] C. D. Capano,[8] E. Capocasa,[30] F. Carbognani,[34] S. Caride,[71] J. Casanueva Diaz,[23] C. Casentini,[25,13] S. Caudill,[16] M. Cavaglià,[21] F. Cavalier,[23] R. Cavalieri,[34] G. Cella,[19] C. B. Cepeda,[1] L. Cerboni Baiardi,[56,57] G. Cerretani,[18,19] E. Cesarini,[25,13] R. Chakraborty,[1] T. Chalermsongsak,[1] S. J. Chamberlin,[72] M. Chan,[36] S. Chao,[73] P. Charlton,[74] E. Chassande-Mottin,[30] H. Y. Chen,[75] Y. Chen,[76] C. Cheng,[73] A. Chincarini,[46] A. Chiummo,[34] H. S. Cho,[77] M. Cho,[62] J. H. Chow,[20] N. Christensen,[78] Q. Chu,[50] S. Chua,[59] S. Chung,[50] G. Ciani,[5] F. Clara,[37] J. A. Clark,[63] J. H. Clayton,[16] F. Cleva,[52] E. Coccia,[25,12,13] P.-F. Cohadon,[59] T. Cokelaer,[91] A. Colla,[79,28] C. G. Collette,[80] L. Cominsky,[81] M. Constancio Jr.,[11] A. Conte,[79,28] L. Conti,[42] D. Cook,[37] T. R. Corbitt,[2] N. Cornish,[31] A. Corsi,[71] S. Cortese,[34] C. A. Costa,[11] M. W. Coughlin,[78] S. B. Coughlin,[82] J.-P. Coulon,[52] S. T. Countryman,[39] P. Couvares,[1] E. E. Cowan,[63] D. M. Coward,[50] M. J. Cowart,[6] D. C. Coyne,[1] R. Coyne,[71] K. Craig,[36] J. D. E. Creighton,[16] T. D. Creighton,[85] J. Cripe,[2] S. G. Crowder,[83] A. Cumming,[36] L. Cunningham,[36] E. Cuoco,[34] T. Dal Canton,[8] S. L. Danilishin,[36] S. D'Antonio,[13] K. Danzmann,[17,8] N. S. Darman,[84] V. Dattilo,[34] I. Dave,[47] H. P. Daveloza,[85] M. Davier,[23] G. S. Davies,[36] E. J. Daw,[86] R. Day,[34] S. De,[35] D. DeBra,[40] G. Debreczeni,[38] J. Degallaix,[65] M. De Laurentis,[67,4] S. Deléglise,[59] W. Del Pozzo,[44] T. Denker,[8,17] T. Dent,[8] H. Dereli,[52] V. Dergachev,[1] R. T. DeRosa,[6] R. De Rosa,[67,4] R. DeSalvo,[87] S. Dhurandhar,[14] M. C. Díaz,[85] A. Dietz,[21] L. Di Fiore,[4] M. Di Giovanni,[79,28] A. Di Lieto,[18,19] S. Di Pace,[79,28] I. Di Palma,[29,8] A. Di Virgilio,[19] G. Dojcinoski,[88] V. Dolique,[65] F. Donovan,[10] K. L. Dooley,[21] S. Doravari,[6,8] R. Douglas,[36] T. P. Downes,[16] M. Drago,[8,89,90] R. W. P. Drever,[1] J. C. Driggers,[37] Z. Du,[70] M. Ducrot,[7] S. E. Dwyer,[37] T. B. Edo,[86] M. C. Edwards,[78] A. Effler,[6] H.-B. Eggenstein,[8] P. Ehrens,[1] J. Eichholz,[5] S. S. Eikenberry,[5] W. Engels,[76] R. C. Essick,[10] T. Etzel,[1] M. Evans,[10] T. M. Evans,[6] R. Everett,[72] M. Factourovich,[39] V. Fafone,[25,13,12] H. Fair,[35] S. Fairhurst,[91] X. Fan,[70] Q. Fang,[50] S. Farinon,[46] B. Farr,[75] W. M. Farr,[44] M. Favata,[88] M. Fays,[91] H. Fehrmann,[8] M. M. Fejer,[40] I. Ferrante,[18,19] E. C. Ferreira,[11] F. Ferrini,[34] F. Fidecaro,[18,19] I. Fiori,[34] D. Fiorucci,[30] R. P. Fisher,[35] R. Flaminio,[65,92] M. Fletcher,[36] N. Fotopoulos,[1] J.-D. Fournier,[52] S. Franco,[23] S. Frasca,[79,28] F. Frasconi,[19] M. Frei,[112] Z. Frei,[53] A. Freise,[44] R. Frey,[58] V. Frey,[23] T. T. Fricke,[8] P. Fritschel,[10] V. V. Frolov,[6] P. Fulda,[5] M. Fyffe,[6] H. A. G. Gabbard,[21] J. R. Gair,[93] L. Gammaitoni,[32,33] S. G. Gaonkar,[14] F. Garufi,[67,4] A. Gatto,[30] G. Gaur,[94,95] N. Gehrels,[68] G. Gemme,[46] B. Gendre,[52] E. Genin,[34] A. Gennai,[19] J. George,[47] L. Gergely,[96] V. Germain,[7] A. Ghosh,[15] S. Ghosh,[51,9] J. A. Giaime,[2,6] K. D. Giardina,[6] A. Giazotto,[19] K. Gill,[97] A. Glaefke,[36] E. Goetz,[98] R. Goetz,[5] L. M. Goggin,[16] L. Gondan,[53] G. González,[2] J. M. Gonzalez Castro,[18,19] A. Gopakumar,[99] N. A. Gordon,[36] M. L. Gorodetsky,[48] S. E. Gossan,[1] M. Gosselin,[34] R. Gouaty,[7] C. Graef,[36] P. B. Graff,[62] M. Granata,[65] A. Grant,[36] S. Gras,[10] C. Gray,[37] G. Greco,[56,57] A. C. Green,[44] P. Groot,[51] H. Grote,[8] S. Grunewald,[29] G. M. Guidi,[56,57] X. Guo,[70] A. Gupta,[14] M. K. Gupta,[95] K. E. Gushwa,[1] E. K. Gustafson,[1] R. Gustafson,[98] J. J. Hacker,[22] B. R. Hall,[55] E. D. Hall,[1] G. Hammond,[36] M. Haney,[99] M. M. Hanke,[8] J. Hanks,[37] C. Hanna,[72] M. D. Hannam,[91] J. Hanson,[6] T. Hardwick,[2] J. Harms,[56,57] G. M. Harry,[100] I. W. Harry,[29] M. J. Hart,[36] M. T. Hartman,[5] C.-J. Haster,[44] K. Haughian,[36] A. Heidmann,[59] M. C. Heintze,[5,6] H. Heitmann,[52] P. Hello,[23] G. Hemming,[34] M. Hendry,[36] I. S. Heng,[36] J. Hennig,[36] A. W. Heptonstall,[1] M. Heurs,[8,17] S. Hild,[36] D. Hoak,[101] K. A. Hodge,[1] D. Hofman,[65] S. E. Hollitt,[102] K. Holt,[6] D. E. Holz,[75] P. Hopkins,[91] D. J. Hosken,[102] J. Hough,[36] E. A. Houston,[36] E. J. Howell,[50] Y. M. Hu,[36] S. Huang,[73] E. A. Huerta,[103,82] D. Huet,[23] B. Hughey,[97] S. Husa,[66] S. H. Huttner,[36] T. Huynh-Dinh,[6] A. Idrisy,[72] N. Indik,[8] D. R. Ingram,[37] R. Inta,[71] H. N. Isa,[36] J.-M. Isac,[59] M. Isi,[1] G. Islas,[22] T. Isogai,[10] B. R. Iyer,[15] K. Izumi,[37] T. Jacqmin,[59] H. Jang,[77] K. Jani,[63] P. Jaranowski,[104] S. Jawahar,[105] F. Jiménez-Forteza,[66] W. W. Johnson,[2] D. I. Jones,[26]

G. Jones,[91] R. Jones,[36] R. J. G. Jonker,[9] L. Ju,[50] Haris K.,[106] C. V. Kalaghatgi,[24,91] V. Kalogera,[82] S. Kandhasamy,[21] G. Kang,[77] J. B. Kanner,[1] S. Karki,[58] M. Kasprzack,[2,23,34] E. Katsavounidis,[10] W. Katzman,[6] S. Kaufer,[17] T. Kaur,[50] K. Kawabe,[37] F. Kawazoe,[8,17] F. Kéfélian,[52] M. S. Kehl,[69] D. Keitel,[8,66] D. B. Kelley,[35] W. Kells,[1] D. G. Keppel,[8] R. Kennedy,[86] J. S. Key,[85] A. Khalaidovski,[8] F. Y. Khalili,[48] I. Khan,[12] S. Khan,[91] Z. Khan,[95] E. A. Khazanov,[107] N. Kijbunchoo,[37] C. Kim,[77] J. Kim,[108] K. Kim,[109] Nam-Gyu Kim,[77] Namjun Kim,[40] Y.-M. Kim,[108] E. J. King,[102] P. J. King,[37] D. L. Kinzel,[6] J. S. Kissel,[37] L. Kleybolte,[27] S. Klimenko,[5] S. M. Koehlenbeck,[8] K. Kokeyama,[2] S. Koley,[9] V. Kondrashov,[1] A. Kontos,[10] M. Korobko,[27] W. Z. Korth,[1] I. Kowalska,[60] D. B. Kozak,[1] V. Kringel,[8] B. Krishnan,[8] A. Królak,[110,111] C. Krueger,[17] G. Kuehn,[8] P. Kumar,[69] L. Kuo,[73] A. Kutynia,[110] B. D. Lackey,[35] M. Landry,[37] J. Lange,[112] B. Lantz,[40] P. D. Lasky,[113] A. Lazzarini,[1] C. Lazzaro,[63,42] P. Leaci,[29,79,28] S. Leavey,[36] E. O. Lebigot,[30,70] C. H. Lee,[108] H. K. Lee,[109] H. M. Lee,[114] K. Lee,[36] A. Lenon,[35] M. Leonardi,[89,90] J. R. Leong,[8] N. Leroy,[23] N. Letendre,[7] Y. Levin,[113] B. M. Levine,[37] T. G. F. Li,[1] A. Libson,[10] T. B. Littenberg,[115] N. A. Lockerbie,[105] J. Logue,[36] A. L. Lombardi,[101] J. E. Lord,[35] M. Lorenzini,[12,13] V. Loriette,[116] M. Lormand,[6] G. Losurdo,[57] J. D. Lough,[8,17] H. Lück,[17,8] A. P. Lundgren,[8] J. Luo,[78] R. Lynch,[10] Y. Ma,[50] T. MacDonald,[40] B. Machenschalk,[8] M. MacInnis,[10] D. M. Macleod,[2] F. Magaña-Sandoval,[35] R. M. Magee,[55] M. Mageswaran,[1] E. Majorana,[28] I. Maksimovic,[116] V. Malvezzi,[25,13] N. Man,[52] I. Mandel,[44] V. Mandic,[83] V. Mangano,[36] G. L. Mansell,[20] M. Manske,[16] M. Mantovani,[34] F. Marchesoni,[117,33] F. Marion,[7] S. Márka,[39] Z. Márka,[39] A. S. Markosyan,[40] E. Maros,[1] F. Martelli,[56,57] L. Martellini,[52] I. W. Martin,[36] R. M. Martin,[5] D. V. Martynov,[1] J. N. Marx,[1] K. Mason,[10] A. Masserot,[7] T. J. Massinger,[35] M. Masso-Reid,[36] F. Matichard,[10] L. Matone,[39] N. Mavalvala,[10] N. Mazumder,[55] G. Mazzolo,[8] R. McCarthy,[37] D. E. McClelland,[20] S. McCormick,[6] S. C. McGuire,[118] G. McIntyre,[1] J. McIver,[1] D. J. A. McKechan,[91] D. J. McManus,[20] S. T. McWilliams,[103] D. Meacher,[72] G. D. Meadors,[29,8] J. Meidam,[9] A. Melatos,[84] G. Mendell,[37] D. Mendoza-Gandara,[8] R. A. Mercer,[16] E. Merilh,[37] M. Merzougui,[52] S. Meshkov,[1] E. Messaritaki,[1] C. Messenger,[36] C. Messick,[72] P. M. Meyers,[83] F. Mezzani,[28,79] H. Miao,[44] C. Michel,[65] H. Middleton,[44] E. E. Mikhailov,[119] L. Milano,[67,4] J. Miller,[10] M. Millhouse,[31] Y. Minenkov,[13] J. Ming,[29,8] S. Mirshekari,[120] C. Mishra,[15] S. Mitra,[14] V. P. Mitrofanov,[48] G. Mitselmakher,[5] R. Mittleman,[10] A. Moggi,[19] M. Mohan,[34] S. R. P. Mohapatra,[10] M. Montani,[56,57] B. C. Moore,[88] C. J. Moore,[121] D. Moraru,[37] G. Moreno,[37] S. R. Morriss,[85] K. Mossavi,[8] B. Mours,[7] C. M. Mow-Lowry,[44] C. L. Mueller,[5] G. Mueller,[5] A. W. Muir,[91] Arunava Mukherjee,[15] D. Mukherjee,[16] S. Mukherjee,[85] N. Mukund,[14] A. Mullavey,[6] J. Munch,[102] D. J. Murphy,[39] P. G. Murray,[36] A. Mytidis,[5] I. Nardecchia,[25,13] L. Naticchioni,[79,28] R. K. Nayak,[122] V. Necula,[5] K. Nedkova,[101] G. Nelemans,[51,9] M. Neri,[45,46] A. Neunzert,[98] G. Newton,[36] T. T. Nguyen,[20] A. B. Nielsen,[8] S. Nissanke,[51,9] A. Nitz,[8] F. Nocera,[34] D. Nolting,[6] M. E. Normandin,[85] L. K. Nuttall,[35] J. Oberling,[37] E. Ochsner,[16] J. O'Dell,[123] E. Oelker,[10] G. H. Ogin,[124] J. J. Oh,[125] S. H. Oh,[125] F. Ohme,[91] M. Oliver,[66] P. Oppermann,[8] Richard J. Oram,[6] B. O'Reilly,[6] R. O'Shaughnessy,[112] D. J. Ottaway,[102] R. S. Ottens,[5] H. Overmier,[6] B. J. Owen,[71] A. Pai,[106] S. A. Pai,[47] J. R. Palamos,[58] O. Palashov,[107] C. Palomba,[28] A. Pal-Singh,[27] H. Pan,[73] Y. Pan,[62] C. Pankow,[82] F. Pannarale,[91] B. C. Pant,[47] F. Paoletti,[34,19] A. Paoli,[34] M. A. Papa,[29,16,8] H. R. Paris,[40] W. Parker,[6] D. Pascucci,[36] A. Pasqualetti,[34] R. Passaquieti,[18,19] D. Passuello,[19] B. Patricelli,[18,19] Z. Patrick,[40] B. L. Pearlstone,[36] M. Pedraza,[1] R. Pedurand,[65] L. Pekowsky,[35] A. Pele,[6] S. Penn,[126] A. Perreca,[1] M. Phelps,[36] O. Piccinni,[79,28] M. Pichot,[52] F. Piergiovanni,[56,57] V. Pierro,[87] G. Pillant,[34] L. Pinard,[65] I. M. Pinto,[87] M. Pitkin,[36] R. Poggiani,[18,19] P. Popolizio,[34] A. Post,[8] J. Powell,[36] J. Prasad,[14] V. Predoi,[91] S. S. Premachandra,[113] T. Prestegard,[83] L. R. Price,[1] M. Prijatelj,[34] M. Principe,[87] S. Privitera,[29] G. A. Prodi,[89,90] L. Prokhorov,[48] O. Puncken,[8] M. Punturo,[33] P. Puppo,[28] M. Pürrer,[29] H. Qi,[16] J. Qin,[50] V. Quetschke,[85] E. A. Quintero,[1] R. Quitzow-James,[58] F. J. Raab,[37] D. S. Rabeling,[20] H. Radkins,[37] P. Raffai,[53] S. Raja,[47] M. Rakhmanov,[85] P. Rapagnani,[79,28] V. Raymond,[29] M. Razzano,[18,19] V. Re,[25] J. Read,[22] C. M. Reed,[37] T. Regimbau,[52] L. Rei,[46] S. Reid,[49] D. H. Reitze,[1,5] H. Rew,[119] S. D. Reyes,[35] F. Ricci,[79,28] K. Riles,[98] N. A. Robertson,[1,36] R. Robie,[36] F. Robinet,[23] C. Robinson,[62] A. Rocchi,[13] A. C. Rodriguez,[2] L. Rolland,[7] J. G. Rollins,[1] V. J. Roma,[58] R. Romano,[3,4] G. Romanov,[119] J. H. Romie,[6] D. Rosińska,[127,43] S. Rowan,[36] A. Rüdiger,[8] P. Ruggi,[34] K. Ryan,[37] S. Sachdev,[1] T. Sadecki,[37] L. Sadeghian,[16] L. Salconi,[34] M. Saleem,[106] F. Salemi,[8] A. Samajdar,[122] L. Sammut,[84,113] E. J. Sanchez,[1] V. Sandberg,[37] B. Sandeen,[82] J. R. Sanders,[98,35] L. Santamaría,[1] B. Sassolas,[65] B. S. Sathyaprakash,[91] P. R. Saulson,[35] O. Sauter,[98] R. L. Savage,[37] A. Sawadsky,[17] P. Schale,[58] R. Schilling,[8,†] J. Schmidt,[8] P. Schmidt,[1,76] R. Schnabel,[27] R. M. S. Schofield,[58] A. Schönbeck,[27] E. Schreiber,[8] D. Schuette,[8,17] B. F. Schutz,[91,29] J. Scott,[36] S. M. Scott,[20] D. Sellers,[6] A. S. Sengupta,[94] D. Sentenac,[34] V. Sequino,[25,13] A. Sergeev,[107] G. Serna,[22] Y. Setyawati,[51,9] A. Sevigny,[37] D. A. Shaddock,[20] S. Shah,[51,9] M. S. Shahriar,[82] M. Shaltev,[8] Z. Shao,[1] B. Shapiro,[40] P. Shawhan,[62] A. Sheperd,[16] D. H. Shoemaker,[10] D. M. Shoemaker,[63] K. Siellez,[52,63] X. Siemens,[16] D. Sigg,[37] A. D. Silva,[11] D. Simakov,[8] A. Singer,[1] L. P. Singer,[68] A. Singh,[29,8] R. Singh,[2]

A. Singhal,[12] A. M. Sintes,[66] B. J. J. Slagmolen,[20] J. R. Smith,[22] N. D. Smith,[1] R. J. E. Smith,[1] E. J. Son,[125] B. Sorazu,[36] F. Sorrentino,[46] T. Souradeep,[14] A. K. Srivastava,[95] A. Staley,[39] M. Steinke,[8] J. Steinlechner,[36] S. Steinlechner,[36] D. Steinmeyer,[8,17] B. C. Stephens,[16] R. Stone,[85] K. A. Strain,[36] N. Straniero,[65] G. Stratta,[56,57] N. A. Strauss,[78] S. Strigin,[48] R. Sturani,[120] A. L. Stuver,[6] T. Z. Summerscales,[128] L. Sun,[84] P. J. Sutton,[91] B. L. Swinkels,[34] M. J. Szczepańczyk,[97] M. Tacca,[30] D. Talukder,[58] D. B. Tanner,[5] M. Tápai,[96] S. P. Tarabrin,[8] A. Taracchini,[29] R. Taylor,[1] T. Theeg,[8] M. P. Thirugnanasambandam,[1] E. G. Thomas,[44] M. Thomas,[6] P. Thomas,[37] K. A. Thorne,[6] K. S. Thorne,[76] E. Thrane,[113] S. Tiwari,[12] V. Tiwari,[91] K. V. Tokmakov,[105] C. Tomlinson,[86] M. Tonelli,[18,19] C. V. Torres,[85,†] C. I. Torrie,[1] D. Töyrä,[44] F. Travasso,[32,33] G. Traylor,[6] D. Trifirò,[21] M. C. Tringali,[89,90] L. Trozzo,[129,19] M. Tse,[10] M. Turconi,[52] D. Tuyenbayev,[85] D. Ugolini,[130] C. S. Unnikrishnan,[99] A. L. Urban,[16] S. A. Usman,[35] H. Vahlbruch,[17] G. Vajente,[1] G. Valdes,[85] N. van Bakel,[9] M. van Beuzekom,[9] J. F. J. van den Brand,[61,9] C. Van Den Broeck,[9] D. C. Vander-Hyde,[35,22] L. van der Schaaf,[9] J. V. van Heijningen,[9] A. A. van Veggel,[36] M. Vardaro,[41,42] S. Vass,[1] M. Vasúth,[38] R. Vaulin,[10] A. Vecchio,[44] G. Vedovato,[42] J. Veitch,[44] P. J. Veitch,[102] K. Venkateswara,[131] D. Verkindt,[7] F. Vetrano,[56,57] A. Viceré,[56,57] S. Vinciguerra,[44] D. J. Vine,[49] J.-Y. Vinet,[52] S. Vitale,[10] T. Vo,[35] H. Vocca,[32,33] C. Vorvick,[37] D. Voss,[5] W. D. Vousden,[44] S. P. Vyatchanin,[48] A. R. Wade,[20] L. E. Wade,[132] M. Wade,[132] M. Walker,[2] L. Wallace,[1] S. Walsh,[16,8,29] G. Wang,[12] H. Wang,[44] M. Wang,[44] X. Wang,[70] Y. Wang,[50] R. L. Ward,[20] J. Warner,[37] M. Was,[7] B. Weaver,[37] L.-W. Wei,[52] M. Weinert,[8] A. J. Weinstein,[1] R. Weiss,[10] T. Welborn,[6] L. Wen,[50] P. Weßels,[8] M. West,[35] T. Westphal,[8] K. Wette,[8] J. T. Whelan,[112,8] D. J. White,[86] B. F. Whiting,[5] K. Wiesner,[8] R. D. Williams,[1] A. R. Williamson,[91] J. L. Willis,[133] B. Willke,[17,8] M. H. Wimmer,[8,17] W. Winkler,[8] C. C. Wipf,[1] A. G. Wiseman,[16] H. Wittel,[8,17] G. Woan,[36] J. Worden,[37] J. L. Wright,[36] G. Wu,[6] J. Yablon,[82] W. Yam,[10] H. Yamamoto,[1] C. C. Yancey,[62] M. J. Yap,[20] H. Yu,[10] M. Yvert,[7] A. Zadrożny,[110] L. Zangrando,[42] M. Zanolin,[97] J.-P. Zendri,[42] M. Zevin,[82] F. Zhang,[10] L. Zhang,[1] M. Zhang,[119] Y. Zhang,[112] C. Zhao,[50] M. Zhou,[82] Z. Zhou,[82] X. J. Zhu,[50] M. E. Zucker,[1,10] S. E. Zuraw,[101] and J. Zweizig[1]

(LIGO Scientific Collaboration and Virgo Collaboration)

[1]*LIGO, California Institute of Technology, Pasadena, California 91125, USA*
[2]*Louisiana State University, Baton Rouge, Louisiana 70803, USA*
[3]*Università di Salerno, Fisciano, I-84084 Salerno, Italy*
[4]*INFN, Sezione di Napoli, Complesso Universitario di Monte S. Angelo, I-80126 Napoli, Italy*
[5]*University of Florida, Gainesville, Florida 32611, USA*
[6]*LIGO Livingston Observatory, Livingston, Louisiana 70754, USA*
[7]*Laboratoire d'Annecy-le-Vieux de Physique des Particules (LAPP), Université Savoie Mont Blanc, CNRS/IN2P3, F-74941 Annecy-le-Vieux, France*
[8]*Albert-Einstein-Institut, Max-Planck-Institut für Gravitationsphysik, D-30167 Hannover, Germany*
[9]*Nikhef, Science Park, 1098 XG Amsterdam, Netherlands*
[10]*LIGO, Massachusetts Institute of Technology, Cambridge, Massachusetts 02139, USA*
[11]*Instituto Nacional de Pesquisas Espaciais, 12227-010 São José dos Campos, São Paulo, Brazil*
[12]*INFN, Gran Sasso Science Institute, I-67100 L'Aquila, Italy*
[13]*INFN, Sezione di Roma Tor Vergata, I-00133 Roma, Italy*
[14]*Inter-University Centre for Astronomy and Astrophysics, Pune 411007, India*
[15]*International Centre for Theoretical Sciences, Tata Institute of Fundamental Research, Bangalore 560012, India*
[16]*University of Wisconsin-Milwaukee, Milwaukee, Wisconsin 53201, USA*
[17]*Leibniz Universität Hannover, D-30167 Hannover, Germany*
[18]*Università di Pisa, I-56127 Pisa, Italy*
[19]*INFN, Sezione di Pisa, I-56127 Pisa, Italy*
[20]*Australian National University, Canberra, Australian Capital Territory 0200, Australia*
[21]*The University of Mississippi, University, Mississippi 38677, USA*
[22]*California State University Fullerton, Fullerton, California 92831, USA*
[23]*LAL, Université Paris-Sud, CNRS/IN2P3, Université Paris-Saclay, 91400 Orsay, France*
[24]*Chennai Mathematical Institute, Chennai 603103, India*
[25]*Università di Roma Tor Vergata, I-00133 Roma, Italy*
[26]*University of Southampton, Southampton SO17 1BJ, United Kingdom*
[27]*Universität Hamburg, D-22761 Hamburg, Germany*
[28]*INFN, Sezione di Roma, I-00185 Roma, Italy*
[29]*Albert-Einstein-Institut, Max-Planck-Institut für Gravitationsphysik, D-14476 Potsdam-Golm, Germany*

[30]*APC, AstroParticule et Cosmologie, Université Paris Diderot, CNRS/IN2P3, CEA/Irfu, Observatoire de Paris, Sorbonne Paris Cité, F-75205 Paris Cedex 13, France*
[31]*Montana State University, Bozeman, Montana 59717, USA*
[32]*Università di Perugia, I-06123 Perugia, Italy*
[33]*INFN, Sezione di Perugia, I-06123 Perugia, Italy*
[34]*European Gravitational Observatory (EGO), I-56021 Cascina, Pisa, Italy*
[35]*Syracuse University, Syracuse, New York 13244, USA*
[36]*SUPA, University of Glasgow, Glasgow G12 8QQ, United Kingdom*
[37]*LIGO Hanford Observatory, Richland, Washington 99352, USA*
[38]*Wigner RCP, RMKI, H-1121 Budapest, Konkoly Thege Miklós út 29-33, Hungary*
[39]*Columbia University, New York, New York 10027, USA*
[40]*Stanford University, Stanford, California 94305, USA*
[41]*Università di Padova, Dipartimento di Fisica e Astronomia, I-35131 Padova, Italy*
[42]*INFN, Sezione di Padova, I-35131 Padova, Italy*
[43]*CAMK-PAN, 00-716 Warsaw, Poland*
[44]*University of Birmingham, Birmingham B15 2TT, United Kingdom*
[45]*Università degli Studi di Genova, I-16146 Genova, Italy*
[46]*INFN, Sezione di Genova, I-16146 Genova, Italy*
[47]*RRCAT, Indore MP 452013, India*
[48]*Faculty of Physics, Lomonosov Moscow State University, Moscow 119991, Russia*
[49]*SUPA, University of the West of Scotland, Paisley PA1 2BE, United Kingdom*
[50]*University of Western Australia, Crawley, Western Australia 6009, Australia*
[51]*Department of Astrophysics/IMAPP, Radboud University Nijmegen, 6500 GL Nijmegen, Netherlands*
[52]*Artemis, Université Côte d'Azur, CNRS, Observatoire Côte d'Azur, CS 34229, Nice cedex 4, France*
[53]*MTA Eötvös University, "Lendulet" Astrophysics Research Group, Budapest 1117, Hungary*
[54]*Institut de Physique de Rennes, CNRS, Université de Rennes 1, F-35042 Rennes, France*
[55]*Washington State University, Pullman, Washington 99164, USA*
[56]*Università degli Studi di Urbino "Carlo Bo," I-61029 Urbino, Italy*
[57]*INFN, Sezione di Firenze, I-50019 Sesto Fiorentino, Firenze, Italy*
[58]*University of Oregon, Eugene, Oregon 97403, USA*
[59]*Laboratoire Kastler Brossel, UPMC-Sorbonne Universités, CNRS, ENS-PSL Research University, Collège de France, F-75005 Paris, France*
[60]*Astronomical Observatory Warsaw University, 00-478 Warsaw, Poland*
[61]*VU University Amsterdam, 1081 HV Amsterdam, Netherlands*
[62]*University of Maryland, College Park, Maryland 20742, USA*
[63]*Center for Relativistic Astrophysics and School of Physics, Georgia Institute of Technology, Atlanta, Georgia 30332, USA*
[64]*Institut Lumière Matière, Université de Lyon, Université Claude Bernard Lyon 1, UMR CNRS 5306, 69622 Villeurbanne, France*
[65]*Laboratoire des Matériaux Avancés (LMA), IN2P3/CNRS, Université de Lyon, F-69622 Villeurbanne, Lyon, France*
[66]*Universitat de les Illes Balears, IAC3—IEEC, E-07122 Palma de Mallorca, Spain*
[67]*Università di Napoli "Federico II," Complesso Universitario di Monte S. Angelo, I-80126 Napoli, Italy*
[68]*NASA/Goddard Space Flight Center, Greenbelt, Maryland 20771, USA*
[69]*Canadian Institute for Theoretical Astrophysics, University of Toronto, Toronto, Ontario M5S 3H8, Canada*
[70]*Tsinghua University, Beijing 100084, China*
[71]*Texas Tech University, Lubbock, Texas 79409, USA*
[72]*The Pennsylvania State University, University Park, Pennsylvania 16802, USA*
[73]*National Tsing Hua University, Hsinchu City, 30013 Taiwan, Republic of China*
[74]*Charles Sturt University, Wagga Wagga, New South Wales 2678, Australia*
[75]*University of Chicago, Chicago, Illinois 60637, USA*
[76]*Caltech CaRT, Pasadena, California 91125, USA*
[77]*Korea Institute of Science and Technology Information, Daejeon 305-806, Korea*
[78]*Carleton College, Northfield, Minnesota 55057, USA*
[79]*Università di Roma "La Sapienza," I-00185 Roma, Italy*
[80]*University of Brussels, Brussels 1050, Belgium*
[81]*Sonoma State University, Rohnert Park, California 94928, USA*
[82]*Northwestern University, Evanston, Illinois 60208, USA*
[83]*University of Minnesota, Minneapolis, Minnesota 55455, USA*

[84]The University of Melbourne, Parkville, Victoria 3010, Australia
[85]The University of Texas Rio Grande Valley, Brownsville, Texas 78520, USA
[86]The University of Sheffield, Sheffield S10 2TN, United Kingdom
[87]University of Sannio at Benevento, I-82100 Benevento, Italy and INFN, Sezione di Napoli, I-80100 Napoli, Italy
[88]Montclair State University, Montclair, New Jersey 07043, USA
[89]Università di Trento, Dipartimento di Fisica, I-38123 Povo, Trento, Italy
[90]INFN, Trento Institute for Fundamental Physics and Applications, I-38123 Povo, Trento, Italy
[91]Cardiff University, Cardiff CF24 3AA, United Kingdom
[92]National Astronomical Observatory of Japan, 2-21-1 Osawa, Mitaka, Tokyo 181-8588, Japan
[93]School of Mathematics, University of Edinburgh, Edinburgh EH9 3FD, United Kingdom
[94]Indian Institute of Technology, Gandhinagar Ahmedabad Gujarat 382424, India
[95]Institute for Plasma Research, Bhat, Gandhinagar 382428, India
[96]University of Szeged, Dóm tér 9, Szeged 6720, Hungary
[97]Embry-Riddle Aeronautical University, Prescott, Arizona 86301, USA
[98]University of Michigan, Ann Arbor, Michigan 48109, USA
[99]Tata Institute of Fundamental Research, Mumbai 400005, India
[100]American University, Washington, D.C. 20016, USA
[101]University of Massachusetts-Amherst, Amherst, Massachusetts 01003, USA
[102]University of Adelaide, Adelaide, South Australia 5005, Australia
[103]West Virginia University, Morgantown, West Virginia 26506, USA
[104]University of Białystok, 15-424 Białystok, Poland
[105]SUPA, University of Strathclyde, Glasgow G1 1XQ, United Kingdom
[106]IISER-TVM, CET Campus, Trivandrum Kerala 695016, India
[107]Institute of Applied Physics, Nizhny Novgorod 603950, Russia
[108]Pusan National University, Busan 609-735, Korea
[109]Hanyang University, Seoul 133-791, Korea
[110]NCBJ, 05-400 Świerk-Otwock, Poland
[111]IM-PAN, 00-956 Warsaw, Poland
[112]Rochester Institute of Technology, Rochester, New York 14623, USA
[113]Monash University, Victoria 3800, Australia
[114]Seoul National University, Seoul 151-742, Korea
[115]University of Alabama in Huntsville, Huntsville, Alabamaa 35899, USA
[116]ESPCI, CNRS, F-75005 Paris, France
[117]Università di Camerino, Dipartimento di Fisica, I-62032 Camerino, Italy
[118]Southern University and A&M College, Baton Rouge, Louisiana 70813, USA
[119]College of William and Mary, Williamsburg, Virginia 23187, USA
[120]Instituto de Física Teórica, University Estadual Paulista/ICTP South American Institute for Fundamental Research, São Paulo São Paulo 01140-070, Brazil
[121]University of Cambridge, Cambridge CB2 1TN, United Kingdom
[122]IISER-Kolkata, Mohanpur, West Bengal 741252, India
[123]Rutherford Appleton Laboratory, HSIC, Chilton, Didcot, Oxon OX11 0QX, United Kingdom
[124]Whitman College, 345 Boyer Avenue, Walla Walla, Washington 99362 USA
[125]National Institute for Mathematical Sciences, Daejeon 305-390, Korea
[126]Hobart and William Smith Colleges, Geneva, New York 14456, USA
[127]Janusz Gil Institute of Astronomy, University of Zielona Góra, 65-265 Zielona Góra, Poland
[128]Andrews University, Berrien Springs, Michigan 49104, USA
[129]Università di Siena, I-53100 Siena, Italy
[130]Trinity University, San Antonio, Texas 78212, USA
[131]University of Washington, Seattle, Washington 98195, USA
[132]Kenyon College, Gambier, Ohio 43022, USA
[133]Abilene Christian University, Abilene, Texas 79699, USA

[†]Deceased.